

Magneto-optical signature of massless Kane electrons in Cd₃As₂

A. Akrap,¹ M. Haki,² S. Tchoumakov,³ I. Crassee,⁴ J. Kuba,^{2,5} M. O. Goerbig,³ C. C. Homes,⁶ O. Caha,⁷ J. Novák,⁷ F. Teppe,⁸ W. Desrat,⁸ S. Koochpayeh,⁹ L. Wu,^{9,10} N. P. Armitage,⁹ A. Nateprov,¹¹ E. Arushanov,¹¹ Q. D. Gibson,¹² R. J. Cava,¹² D. van der Marel,¹ B. A. Piot,² C. Faugeras,² G. Martinez,² M. Potemski,² and M. Orlita^{2,13,*}

¹*DQMP, University of Geneva, CH-1211 Geneva 4, Switzerland*

²*LNCMI, CNRS-UGA-UPS-INSA, 25, avenue des Martyrs, 38042 Grenoble, France*

³*LPS, Univ. Paris-Sud, Univ. Paris-Saclay, CNRS UMR 8502, 91405 Orsay, France*

⁴*GAP-Biophotonics, University of Geneva, CH-1211 Geneva 4, Switzerland*

⁵*CEITEC BUT, Brno University of Technology, 616 00 Brno, Czech Republic*

⁶*CMPMS, Brookhaven National Laboratory, Upton, New York 11973, USA*

⁷*CEITEC MU, Masaryk University, Faculty of Science, 61137 Brno, Czech Republic*

⁸*Laboratoire Charles Coulomb, CNRS, Université Montpellier, 34095 Montpellier, France*

⁹*The Institute for Quantum Matter, The Johns Hopkins University, Baltimore, Maryland 21218, USA*

¹⁰*Department of Physics, University of California, Berkeley, CA 94720 USA*

¹¹*Institute of Applied Physics, Academy of Sciences of Moldova, MD-2028 Chisinau, Moldova*

¹²*Department of Chemistry, Princeton University, Princeton, New Jersey 08544, USA*

¹³*Institute of Physics, Charles University in Prague, 12116 Prague, Czech Republic*

We report on optical reflectivity experiments performed on Cd₃As₂ over a broad range of photon energies and magnetic fields. The observed response clearly indicates the presence of 3D massless charge carriers. The specific cyclotron resonance absorption in the quantum limit implies that we are probing massless Kane electrons rather than symmetry-protected 3D Dirac particles. The latter may appear at a smaller energy scale and are not directly observed in our infrared experiments.

Cadmium arsenide (Cd₃As₂) has recently been identified [1–3] as the premier 3D topological Dirac semimetal stable under ambient conditions, thus inspiring a renewed interest in the electronic properties of this widely investigated compound [4–7]. The current consensus is that the electronic bands of Cd₃As₂ comprise a single pair of symmetry-protected 3D Dirac nodes located in the vicinity of the Γ point of the Brillouin zone. Nevertheless, the exact location, size, anisotropy and tilt of these conical bands still remain a puzzle. Most strikingly, ARPES studies imply cones extending over a few hundred meV [2] or even eV [1]. In contrast, the band inversion estimated in STM/STS experiments [3], in line with recent and past theoretical modeling [5, 8], invokes Dirac cones which extend over an order-of-magnitude smaller energy range.

In this Letter, we clarify the controversies on the electronic bands of Cd₃As₂. Based on our magneto-optical experiments, we argue that the band structure may in fact include two types of conical features, one spread over the large, and the second on the small energy scale. The widely extended conical band results from the standard Kane model [9, 10] applied to a semiconductor with a nearly vanishing band gap, it is not symmetry-protected and it hosts carriers that are referred to as massless Kane electrons [11]. The symmetry-protected Dirac cones, if present in Cd₃As₂ at all, may only appear on a much smaller energy scale, in contrast to conclusions of ARPES studies [1, 2], but in line with the STM/STS data [3].

Our experiments were performed on two bulk Cd₃As₂ n -doped samples with facets oriented using x -ray scattering experiments [12]. The sample with the (001) facet ($\sim 1 \times 2$ mm²) was cut and polished from a bulk crystal

prepared using the technique described in Ref. 13. The (112)-oriented sample ($\sim 2 \times 4$ mm²) was grown using a thermal evaporation method [14].

The reflectance experiments were performed using standard Fourier transform spectroscopy. In experiments at $B = 0$, the reflectivity was measured in the range of 0.003–3 eV using an in situ overcoating technique. Ellipsometry was employed to determine the dielectric function between 0.5 and 4 eV. To measure reflectivity in magnetic fields, a resistive coil was used, with a liquid helium bath cryostat at $T = 1.8$ K, and samples placed in a low-pressure helium exchange gas.

The reflectance spectra taken at $B = 0$ and $T = 5$ K are plotted in Fig. 1a. The observation of characteristic plasma edges indicates the presence of free charge carriers. Sharp phonon response is clearly observed around 15–30 meV. For both samples, the optical conductivity (Fig. 1b) was extracted using the Kramers-Kronig analysis of the reflectivity data, with the phase anchored by the high-frequency ellipsometry data. At first glance, the optical conductivity increases linearly with the photon frequency, which is consistent with the response of 3D massless particles [11, 15]. A closer inspection reveals a slight superlinear increase, which is discussed later on (cf. similar recent data in Ref. 16).

At low energies, the optical conductivity reflects different electron densities in the studied samples, which implies different onsets of interband absorption due to Pauli blocking. These onsets were identified as inflection points in the conductivity spectra and marked by vertical arrows in Fig. 1b. In an ideal conical band, such an onset corresponds to twice the Fermi energy. In Cd₃As₂, these

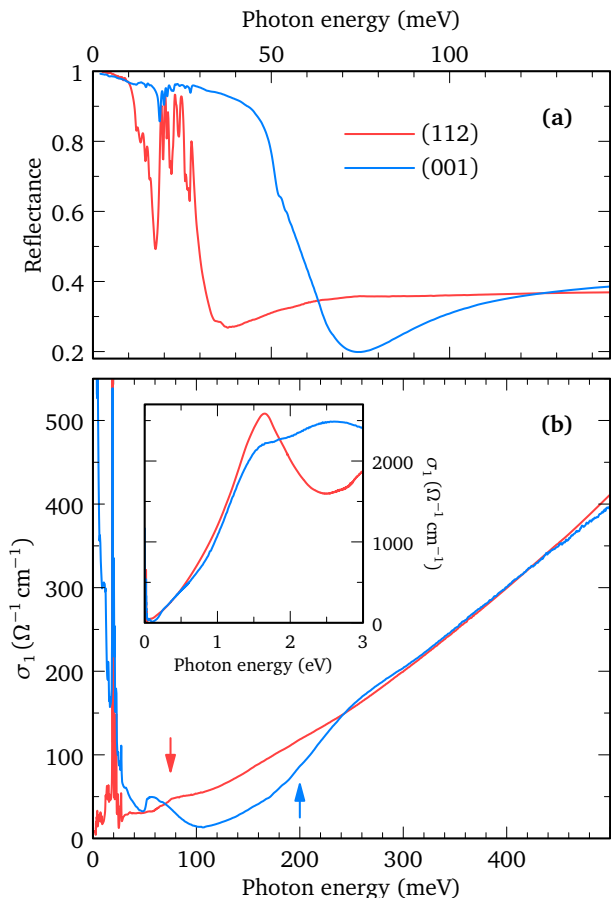


FIG. 1. (color online) (a) The reflectance of both studied samples at 5 K and $B = 0$ dominated by sharp plasma edges and phonon response. For a purely conical band structure, the approximate ratio of plasma frequencies, $\omega_p^{001}/\omega_p^{112} \approx 2$, implies $2\times$ larger E_F , and therefore, $8\times$ higher carrier density ($n \propto E_F^3$) for the (001)-oriented sample. (b) The optical conductivity with a nearly linear dependence on the photon energy. Inset: optical conductivity in a wide energy range.

onsets are closer to E_F , due to the electron-hole asymmetry, as confirmed *a posteriori* by our data analysis. For 3D massless particles, the plasma frequency is predicted to scale linearly with the Fermi energy, $\omega_p \propto E_F$ [17]. Indeed, for our two samples, the onset energy ratio approaches 2 and matches the plasma frequency ratio. At higher photon energies, the optical conductivity indicates a fairly high isotropy of Cd_3As_2 , with the first signs of anisotropy appearing above 0.5 eV (inset of Fig. 1b).

The presence of massless electrons in Cd_3As_2 is also visible in our high-field magneto-reflectivity data (Fig. 2). At low B , the plasma edge undergoes a clear splitting in both samples [12], which is fully consistent with previously published experiments [7] and which can be described using a classical magneto-plasma theory [18] with the quasi-classical cyclotron frequency ω_c linear in B . At high B , for $\omega_c \gg \omega_p$, a well-defined cyclotron resonance (CR) mode appears, likely accompanied by a weaker

satellite line (full and open circles in Figs. 2a,b, respectively). These modes, determined as the corresponding inflection points in the spectra [12], follow a \sqrt{B} dependence (Fig. 2c) – a hallmark of the characteristic spacing of Landau levels (LLs) of massless particles.

The high-field CR absorption confirms the isotropic nature of the conical band structure consistent with the zero-field response. A closer look at the data obtained on samples with differently oriented facets reveals a small difference in the measured CR energies, $\omega_c^{001}/\omega_c^{112} \sim 1.03$ (Fig. 2c). This difference, comparable with the experimental accuracy of the CR energy, indicates a weak anisotropy, $v_\perp/v_\parallel \approx 0.9$, expressed using the in-plane v_\parallel and out-of-plane v_\perp velocity [12].

Let us compare, first on a *qualitative* level, our experimental findings with the electronic band structure expected within the semi-empirical model proposed for Cd_3As_2 by Bodnar [5]. This model extends the standard Kane model [9], widely applied to describe the band structure of zinc-blende (cubic) semiconductors at the Γ point and based on the exact diagonalization of the $\mathbf{k} \cdot \mathbf{p}$ Hamiltonian, using the finite basis of s and p valence states. Bodnar retained the standard Kane parameters (band gap E_g , interband matrix element P and spin-orbit coupling Δ), while additionally introducing the crystal field splitting δ [19]. The latter parameter δ reflects the tetragonal symmetry of Cd_3As_2 and splits the 4-dimensional Γ_8 representation, which in cubic semiconductors corresponds to heavy and light hole bands, degenerate at the Γ point.

The model allows for the existence of two different branches of 3D massless electrons, both having their charge neutrality point at the Fermi energy in an undoped system. For $E_g < 0$ (*i.e.*, in the inverted band gap regime) and $\delta > 0$, the Γ_6 and Γ_7 bands, which originate in the split Γ_8 representation, form an avoided crossing in all momentum directions, except the tetragonal (z) axis, where such an anticrossing is forbidden by symmetry (due to the C_4 rotation axis [20]). As a consequence, two strongly tilted and anisotropic 3D cones are created at $k_z^D = \pm\sqrt{|E_g|\delta/P^2}$ (Fig. 3a,b). This specific behavior was postulated in an earlier work [5] and the cones were later classified as symmetry-protected Dirac cones [8].

Another sort of massless particle appears when both the band gap and crystal field splitting vanish. In this limit, the Bodnar model becomes equivalent to that of massless Kane electrons [10, 11] with a single isotropic spin-degenerate cone at the Γ point (Fig. 3c). This cone is characterized by a velocity $v = \sqrt{2/3}P/\hbar$ and, additionally, by the appearance of a flat heavy-hole band. The anisotropy of this cone may be introduced in the model through an anisotropic matrix element P .

Notably, the Bodnar model generically allows for a crossover from massless Dirac to Kane electrons (Fig. 3b). For positive δ and negative E_g small as compared to Δ , two symmetry-protected Dirac cones are formed at low

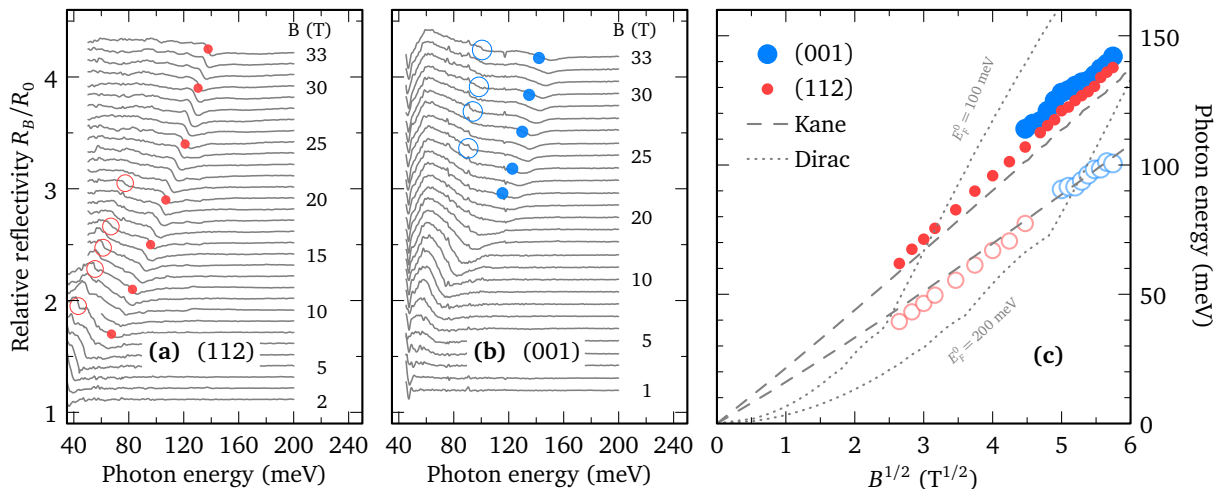


FIG. 2. (color online) Relative magneto-reflectivity spectra of the (112)- and (001)-oriented sample measured at $T = 1.8$ K in (a) and (b), respectively. The observed resonances are marked by full (open) circles for dominant (weak, likely present) CR modes. Their \sqrt{B} dependence is shown in the part (c), together with the theoretical curves based on the Dirac (dotted) and gapless Kane (dashed) models. The former curves were calculated for the velocity 10^6 m/s and the zero-field Fermi energies $E_F^0 = 100$ and 200 meV; the kinks appear due to field-dependence of E_F [12].

energies, with the size comparable to δ . These Dirac cones then merge, above the Lifshitz point, into a single conical band. At higher energies, this single cone is well described by the gapless Kane model and thus hosts particles with a linear dispersion – the so-called massless Kane electrons [11].

The low anisotropy of the observed optical response is the first indication that one is dealing with a single cone of Kane electrons (around the Γ point) rather than two Dirac cones (located along the tetragonal axis at $\pm k_z^D$). More direct evidence comes from the qualitative analysis of our high-field CR data. In the quantum regime, materials with massless electrons imply multi-mode CR absorption. The individual modes correspond to excitations between adjacent non-equidistantly spaced LLs of the same spin, analogous to the CR response of graphene [21]. The intensity of these modes is related to the number of charge carriers in particular LLs, which follows their degeneracy and spacing. We have found two such modes in the response of each Cd_3As_2 sample.

The magneto-reflectivity response of the (112)-oriented sample is dominated by a CR mode, which emerges below $B = 10$ T and remains present up to the highest magnetic field applied, $B = 33$ T (Fig. 2a). In any system of either Dirac or Kane massless electrons, this is only possible when the quantum limit is approached and electrons are excited from the lowest LL in the conduction band. This is because this fundamental level cannot be, in contrast to higher LLs, depopulated with the increasing B .

To test whether 3D Dirac electrons may be at the origin of the observed (isotropic) CR response, let us consider their LL spectrum, $E_n^{\text{Dirac}} = \pm v\sqrt{2e\hbar Bn} + \hbar^2 k^2$. It comprises specific $n = 0$ LLs dispersing linearly with the

momentum k along the magnetic field. Each CR mode between adjacent LLs with $n \geq 1$ is characterized by a singularity in the joint density of states due to the band extrema at $k = 0$, and therefore, by a strict \sqrt{B} dependence. For the fundamental CR mode, which is the only active mode in the quantum limit and corresponds to excitations from the $n = 0$ levels, such a singularity is missing because of the linear dispersion in k (Fig. 4a). Its only characteristic spectral feature is the low-energy absorption edge at $L_{0 \rightarrow 1} = \sqrt{v^2 2e\hbar B} + E_F^0 - E_F$ [22].

Importantly, this low-energy edge does not follow the \sqrt{B} dependence, and moreover, its position depends on E_F . This is in clear disagreement with our experimental findings, where the fundamental CR lines (full circles in Fig. 2c) show a nearly perfect \sqrt{B} dependence and have almost the same position for both studied samples (despite significantly different E_F). The picture of 3D Dirac electrons thus does not match our data. We illustrate this in Fig. 2c by plotting the $L_{0 \rightarrow 1}$ energy for two selected zero-field Fermi levels $E_F^0 = 100$ and 200 meV. These correspond to the chemical potential estimated from the zero-field optical conductivity in Fig. 1b for the two investigated specimens. The field dependence of E_F was calculated supposing a 3D Dirac LL spectrum (see Ref. [12] for further details). The plotted $L_{0 \rightarrow 1}$ curves clearly deviate from the \sqrt{B} dependence and thus cannot be used for fitting by any variation of the velocity parameter (fixed at 10^6 m/s in the plot).

In contrast, $n = 0$ Landau levels dispersing linearly in k are absent in systems with Kane electrons, $E_{\zeta, n, \sigma}^{\text{Kane}} = \zeta v \sqrt{e\hbar B(2n - 1 + \sigma) + \hbar^2 k^2}$, where $\zeta = -1, 0, 1$ and $\sigma = \pm 1/2$ [11]. As a result, all CR modes of Landau-quantized massless Kane electrons, including the funda-

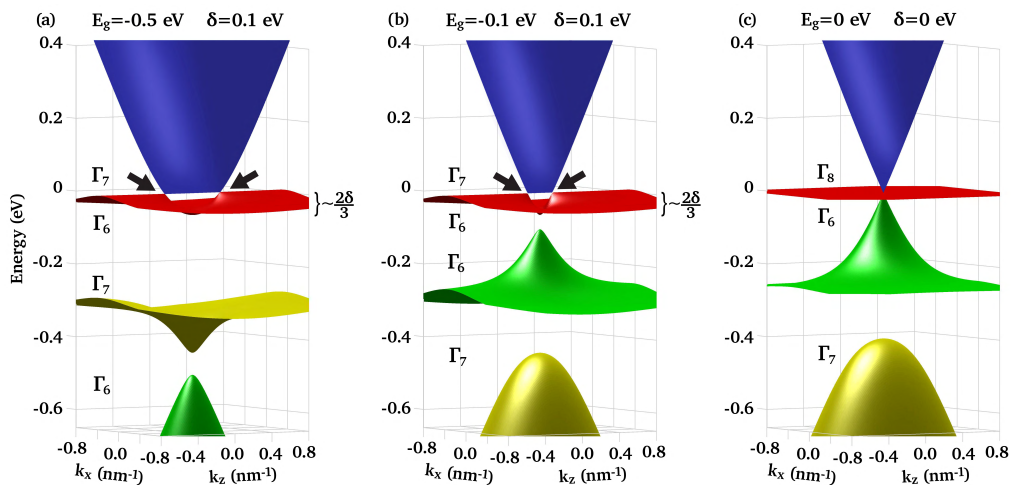


FIG. 3. The band structure calculated using the Bodnar model (at $k_y \equiv 0$) for various E_g and δ chosen to approach (a) ab initio calculations [8], (b) the original Bodnar’s work [5] and (c) Kane electrons [11], and for $\Delta = 400$ meV and $v = 0.93 \times 10^6$ m/s. Two highly tilted Dirac cones (marked by black arrows) with the size comparable to δ appear in (a) and (b) at the crossing points of the upper Γ_7 and Γ_6 bands. The widely extended cone of Kane electrons is visible in (c) and partly also (b).

mental one, follow a \sqrt{B} dependence. Notably, in an electron-doped system, the Fermi energy never drops below the $n = 1^\uparrow$ level and the fundamental mode thus corresponds to $n = 1^\uparrow \rightarrow 2^\uparrow$ (Fig. 4b).

After these qualitative arguments, we now proceed with the *quantitative* analysis of our data, using the simplest gapless Kane model [11]. This model implies only two material parameters, v and Δ . The velocity parameter was taken after Bodnar, $v = 0.93 \times 10^6$ m/s, in perfect agreement with a value recently deduced from STM/STS measurements [3], 0.94×10^6 m/s, determined for a single conical band at the Γ point. The strength of the spin-orbit coupling was set to $\Delta = 400$ meV, the value known for InAs. This choice is justified by the simple fact that the strength of the spin-orbit interaction in most semiconductors is predominantly governed by the anion atom, which in this case is arsenic. Lower values might also be considered (e.g., $\Delta = 270$ meV [5]), at the expense of a slightly increased electron-hole asymmetry in the model.

Figure 2c shows the theoretical positions of the two CR modes expected to be active in the vicinity of the quantum limit of massless Kane electrons (dashed lines). These modes correspond to excitations between the two lowest spin-split Landau levels in the conduction band (from $n = 1$ to 2), as denoted by vertical arrows in Fig. 4b. The Kane model thus fits well the experimental points for the dominant CR line as well as for its weaker satellite, using only the above estimates for v and Δ , introducing no additional fitting parameters. Consistent with this picture, the satellite line is gradually suppressed with B in the lower-doped (112)-oriented sample, when the system enters the quantum limit.

Although the Kane model explains our data fairly well, due to the tetragonal nature of Cd₃As₂ this model cannot

be valid down to arbitrarily low energies. The comparison with the full Bodnar model [12] gives rough estimates (upper limits) for the band gap and crystal field splitting: $E_g = -30$ meV and $\delta = 30$ meV. This choice of parameters is consistent with a band structure similar to the one in Fig. 3b, where 3D Dirac electrons are present but are limited to low energies. This confirms that the (magneto-)optical response studied in our experiments is dominated by the massless Kane and not Dirac electrons.

Having concluded the presence of Kane electrons in Cd₃As₂, we return to the zero-field data (Fig. 1b). The optical conductivity in an ideal undoped system of Kane electrons (for $\Delta \rightarrow \infty$) may be written as $\text{Re}\{\sigma^{\text{Kane}}(\omega)\} = (13/12)\omega e^2 / (4\pi\hbar v)$ [11]. The dominant contribution to this interband absorption stems from excitations from the flat band (red in Fig. 3c) to the upper cone (blue). This may be viewed as interband absorption in the cone with an extreme electron-hole asymmetry and confirms our assignment of the onsets in optical conductivity to E_F (and not $2E_F$). The contribution from the lower (green) cone is weaker mainly due to the $8\times$ smaller joint density of states.

In our case, however, the lower cone flattens significantly when approaching the energy of $-\Delta$ (Figs. 3b,c) and the conductivity should be, in the first approximation, corrected by an additional term [12], which nearly doubles its slope for $\hbar\omega > \Delta$:

$$\text{Re}\{\sigma^{\text{Cd}_3\text{As}_2}(\omega)\} \approx \frac{\omega e^2}{4\pi\hbar v} \left[\frac{13}{12} + \theta(\hbar\omega - \Delta) \left(1 - \frac{\Delta}{\hbar\omega}\right)^2 \right],$$

where $\theta(x)$ is the Heaviside function. This may explain the superlinear increase (upturn) in the spectra around 0.5 eV (Fig. 1b) as a simple band-effect, providing thus

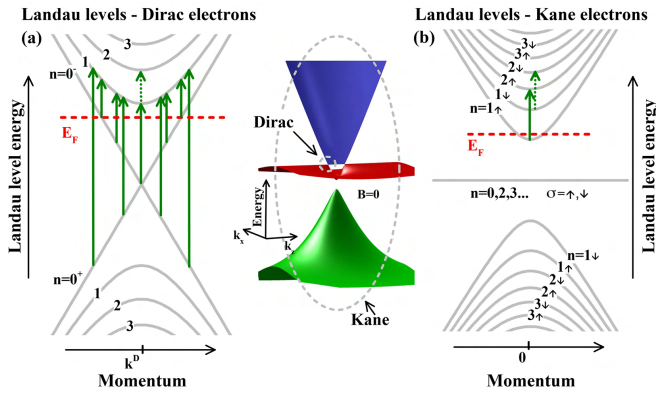


FIG. 4. Idealized Landau levels of (a) Dirac and (b) Kane electrons as occupied in the quantum limit and their relative energy scale in the Bodnar model (central inset). The $n = 0$ LLs typical of Dirac electrons, dispersing linearly with the momentum, are absent for Kane electrons. The solid arrows show CR modes active in the quantum limit, the dashed arrows those which vanish when this limit is reached. For details about the crossover from Dirac- to Kane-like LLs see Ref. 12.

an alternative to the recent interpretation in terms of self-energy corrections within the Dirac picture [16]. One may expect such corrections, as well as enhanced interaction effects, rather at high energies (1 – 2 eV) where the maximum in the optical conductivity hints at an enlarged density of states.

On the other hand, the above expression for conductivity still underestimates the total observed absorption strength. Only semi-quantitative agreement is thus achieved, which points towards other contributions to conductivity. These include, for instance, enhanced absorption at low energies ($\hbar\omega < \Delta$) due to gradually flattened lower cone, as well as excitations into the second conduction band, not included in the Bodnar/Kane model, but expected at energies around ~ 0.5 eV above the flat band [3, 8].

In summary, we have studied bulk Cd_3As_2 by means of optical magneto-spectroscopy, unambiguously showing the presence of 3D massless particles. We conclude that within the investigated range of frequencies and magnetic fields, the observed response is due to massless Kane electrons, the presence of which is fully consistent with the Bodnar model elaborated for this material in the past. This model is, in our opinion, also applicable to study the symmetry-protected 3D Dirac electrons. These may appear in Cd_3As_2 at a small energy scale given by the crystal field splitting (a few ten meV at most). Our finding contradicts the conclusions of ARPES studies [1, 2], in which the observed conical feature extending over a few hundred meV was interpreted in terms of symmetry-protected Dirac particles. Nevertheless, the identified massless Kane electrons should exhibit some properties that are typical of truly relativistic particles, with the Klein tunnelling as a prominent example [23, 24].

This work was supported by ERC MOMB (No. 320590), TWINFUSYON (No. 692034), Lia TeraMIR, TERASENS and by MEYS CEITEC 2020 (No. LQ1601) projects. Support was also received from the U.S. Department of Energy, Office of Basic Energy Sciences, MSE Division and Contract No. DE-SC0012704 (C.C.H.) and DE-FG02-08ER46544 (S.K., L.W. and N.P.A.). A.A. acknowledges funding from the Ambizione grant of the Swiss NSF. Work at Princeton University was supported by the ARO MURI on topological insulators (W911NF-12-0461). The authors acknowledge discussions with D. M. Basko, M. Civelli, and W.-L. Lee.

* milan.orlita@lncmi.cnrs.fr

- [1] Z. Liu *et al.*, *Nature Mater.* **13**, 677 (2014).
- [2] M. Neupane *et al.*, *Nature Comm.* **5**, 3786 (2014); S. Borisenko *et al.*, *Phys. Rev. Lett.* **113**, 027603 (2014).
- [3] S. Jeon *et al.*, *Nature Mater.* **13**, 851 (2014).
- [4] I. Rosenman, *J. Phys. Chem. Solids* **30**, 1385 (1969).
- [5] J. Bodnar, in *Proc. III Conf. Narrow-Gap Semiconductors, Warsaw*, edited by J. Rauhuzkiewicz, M. Górska, and E. Kaczmarek (Elsevier, 1977) p. 311.
- [6] M. Gelten, C. van Es, F. Blom, and J. Jongeneelen, *Solid State Commun.* **33**, 833 (1980); M. J. Aubin, A. Rambo, and E. Arushanov, *Phys. Rev. B* **23**, 3602 (1981); E. Arushanov, *Prog. Cryst. Growth Ch.* **3**, 211 (1980); *Prog. Cryst. Growth Ch.* **25**, 131 (1992).
- [7] H. Schleijsen, M. von Ortenberg, M. Gelten, and F. Blom, *Int. J. Infrared Milli.* **5**, 171 (1984).
- [8] Z. Wang, H. Weng, Q. Wu, X. Dai, and Z. Fang, *Phys. Rev. B* **88**, 125427 (2013).
- [9] E. O. Kane, *J. Phys. Chem. Solids* **1**, 249 (1957).
- [10] P. Kacman and W. Zawadzki, *phys. stat. sol. (b)* **47**, 629 (1971).
- [11] M. Orlita *et al.*, *Nature Phys.* **10**, 233 (2014).
- [12] See Supplementary Materials.
- [13] M. N. Ali *et al.*, *Inorganic Chemistry* **53**, 4062 (2014).
- [14] C. P. Weber *et al.*, *Appl. Phys. Lett.* **106**, 231904 (2015).
- [15] T. Timusk *et al.*, *Phys. Rev. B* **87**, 235121 (2013).
- [16] D. Neubauer *et al.*, *Phys. Rev. B* **93**, 121202 (2016).
- [17] S. Das Sarma and E. H. Hwang, *Phys. Rev. Lett.* **102**, 206412 (2009).
- [18] E. D. Palik and J. Furdyna, *Rep. Prog. Phys.* **33**, 1193 (1970).
- [19] H. Kildal, *Phys. Rev. B* **10**, 5082 (1974).
- [20] B.-J. Yang and N. Nagaosa, *Nature Comm.* **5**, 4898 (2014).
- [21] P. Neugebauer *et al.*, *Phys. Rev. Lett.* **103**, 136403 (2009).
- [22] P. E. C. Ashby and J. P. Carbotte, *Phys. Rev. B* **87**, 245131 (2013).
- [23] M. I. Katsnelson, K. S. Novoselov, and A. K. Geim, *Nature Phys.* **2**, 620 (2006).
- [24] T. Liang *et al.*, *Nature Mater.* **14**, 280 (2015).

Supplementary materials for “Magneto-optical signature of massless Kane electrons in Cd₃As₂”

A. Akrap,¹ M. Haki,² S. Tchoumakov,³ I. Crassee,⁴ J. Kuba,^{2,5} M. O. Goerbig,³ C. C. Homes,⁶ O. Caha,⁷ J. Novák,⁷ F. Teppe,⁸ W. Desrat,⁸ S. Koohpayeh,⁹ L. Wu,^{9,10} N. P. Armitage,⁹ A. Nateprov,¹¹ E. Arushanov,¹¹ Q. D. Gibson,¹² R. J. Cava,¹² D. van der Marel,¹ B. A. Piot,² C. Faugeras,² G. Martinez,² M. Potemski,² and M. Orlita^{2,13,*}

¹*DQMP, University of Geneva, CH-1211 Geneva 4, Switzerland*

²*LNCMI, CNRS-UGA-UPS-INSA, 25, avenue des Martyrs, 38042 Grenoble, France*

³*LPS, Univ. Paris-Sud, Univ. Paris-Saclay, CNRS UMR 8502, 91405 Orsay, France*

⁴*GAP-Biophotonics, University of Geneva, CH-1211 Geneva 4, Switzerland*

⁵*CEITEC BUT, Brno University of Technology, 616 00 Brno, Czech Republic*

⁶*CMPMS, Brookhaven National Laboratory, Upton, New York 11973, USA*

⁷*CEITEC MU, Masaryk University, Faculty of Science, 61137 Brno, Czech Republic*

⁸*Laboratoire Charles Coulomb, CNRS, Université Montpellier, 34095 Montpellier, France*

⁹*The Institute for Quantum Matter, The Johns Hopkins University, Baltimore, Maryland 21218, USA*

¹⁰*Department of Physics, University of California, Berkeley, CA 94720 USA*

¹¹*Institute of Applied Physics, Academy of Sciences of Moldova, MD-2028 Chisinau, Moldova*

¹²*Department of Chemistry, Princeton University, Princeton, New Jersey 08544, USA*

¹³*Institute of Physics, Charles University in Prague, 12116 Prague, Czech Republic*

In the Supplementary Materials provided here we discuss the details of the theoretical calculations and data analysis which have been used in the main text.

BODNAR MODEL – ELECTRONIC BAND STRUCTURE

The model presented for the electronic band structure of Cd₃As₂ [1] – employed by Bodnar for the theoretical analysis of previously reported magneto-transport data (Shubnikov-de Haas oscillations) – closely follows the approach proposed by Kildal for another tetragonal semiconductor CdGeAs₂ [2].

This model extends the standard Kane model [3], which is widely applied to describe the band structure of zinc-blende (cubic) semiconductors at the Γ point and which is based on the exact diagonalization of the $\mathbf{k} \cdot \mathbf{p}$ Hamiltonian, using the finite basis formed from s -type ($|S\rangle$) and p -type ($|X\rangle, |Y\rangle, |Z\rangle$) atomic-like valence states:

$$\begin{aligned} & i|S \downarrow\rangle, 2^{-\frac{1}{2}}|(X - iY) \downarrow\rangle, -2^{-\frac{1}{2}}|(X + iY) \downarrow\rangle, |Z \uparrow\rangle, \\ & i|S \uparrow\rangle, 2^{-\frac{1}{2}}|(X + iY) \uparrow\rangle, 2^{-\frac{1}{2}}|(X - iY) \uparrow\rangle, |Z \downarrow\rangle, \end{aligned}$$

where \uparrow and \downarrow refer to the up and down orientation of spin along z axis, respectively.

In this basis, the Hamiltonian may be written, using the notation $k_{\pm} = (k_x \pm ik_y)/\sqrt{2}$:

$$\hat{H}(\mathbf{k}) = \begin{pmatrix} E_g & P_{\perp}k_{-} & -P_{\perp}k_{+} & 0 & 0 & 0 & 0 & P_{\parallel}k_z \\ P_{\perp}k_{+} & 0 & 0 & 0 & 0 & 0 & 0 & 0 \\ -P_{\perp}k_{-} & 0 & -\frac{2}{3}\Delta & \frac{\sqrt{2}\Delta}{3} & 0 & 0 & 0 & 0 \\ 0 & 0 & \frac{\sqrt{2}\Delta}{3} & -(\delta + \frac{\Delta}{3}) & P_{\parallel}k_z & 0 & 0 & 0 \\ 0 & 0 & 0 & P_{\parallel}k_z & E_g & P_{\perp}k_{+} & P_{\perp}k_{-} & 0 \\ 0 & 0 & 0 & 0 & P_{\perp}k_{-} & 0 & 0 & 0 \\ 0 & 0 & 0 & 0 & P_{\perp}k_{+} & 0 & -\frac{2}{3}\Delta & \frac{\sqrt{2}\Delta}{3} \\ P_{\parallel}k_z & 0 & 0 & 0 & 0 & 0 & \frac{\sqrt{2}\Delta}{3} & -(\delta + \frac{\Delta}{3}) \end{pmatrix}, \quad (S1)$$

where E_g represents the separation between valence and conduction bands (the band gap), Δ is the spin-orbit splitting, δ is crystal-field splitting (due to tetragonal symmetry of Cd₃As₂). P_{\parallel} and P_{\perp} are (anisotropic) interband matrix elements.

The above Hamiltonian can be rewritten as:

$$\hat{H}(\mathbf{k}) = \hat{H}(\mathbf{k} = 0) + P_{\perp}(k_x \hat{J}_x + k_y \hat{J}_y) + P_{\parallel}k_z \hat{J}_z, \quad (S2)$$

The projection of the angular momentum operator \mathbf{J} [4] on an arbitrary direction $\mathbf{n} = (\sin(\theta) \cos(\phi), \sin(\theta) \sin(\phi), \cos(\theta))$, described by spherical coordinates θ, ϕ , can be related to J_z by a rotation:

$$\begin{aligned} \mathbf{J} \cdot \mathbf{n} &= J_x \sin(\theta) \cos(\phi) + J_y \sin(\theta) \sin(\phi) + J_z \cos(\theta) = U_\phi^\dagger (J_x \sin(\theta) + J_z \cos(\theta)) U_\phi \\ &= U_\phi^\dagger U_\theta^\dagger J_z U_\theta U_\phi, \end{aligned} \quad (\text{S3})$$

$$U_\phi = \text{diag}(1, e^{-i\phi}, e^{i\phi}, e^{i\phi}, e^{2i\phi}, 1, 1), \quad (\text{S4})$$

$$U_\theta = \exp(i\theta L), \quad (\text{S5})$$

$$L = \begin{pmatrix} 0 & 0 & 0 & 0 & \frac{i}{2} & 0 & 0 & 0 \\ 0 & 0 & 0 & 0 & 0 & 0 & \frac{i}{2} & \frac{i}{\sqrt{2}} \\ 0 & 0 & 0 & 0 & 0 & -\frac{i}{2} & 0 & -\frac{i}{\sqrt{2}} \\ 0 & 0 & 0 & 0 & 0 & -\frac{i}{\sqrt{2}} & -\frac{i}{\sqrt{2}} & -\frac{i}{2} \\ -\frac{i}{2} & 0 & 0 & 0 & 0 & 0 & 0 & 0 \\ 0 & 0 & \frac{i}{2} & \frac{i}{\sqrt{2}} & 0 & 0 & 0 & 0 \\ 0 & -\frac{i}{2} & 0 & \frac{i}{\sqrt{2}} & 0 & 0 & 0 & 0 \\ 0 & -\frac{i}{\sqrt{2}} & \frac{i}{\sqrt{2}} & \frac{i}{2} & 0 & 0 & 0 & 0 \end{pmatrix}. \quad (\text{S6})$$

For non-zero δ , this rotation commutes with $\hat{H}(\mathbf{k} = 0)$ for any ϕ but only at $\theta = 0$. The tetragonal crystal field δ thus preserves the rotation symmetry along the axis of deformation (z -axis) and along this axis the band crossing is maintained.

The Hamiltonian in Eq. (S1) does not allow one to obtain a simple analytical solution for the electronic band structure. Nevertheless, three selected examples of a numerically calculated band structure are presented in Fig. 3 of the main text. The eigenvalues can be analytically found at least at the Γ point ($\mathbf{k} = \mathbf{0}$) where we obtain doubly (spin) degenerate bands: $E_1 = E_g$, $E_2^{(\pm)} = -(\Delta + \delta)/2 \pm \sqrt{(\Delta - \delta/3)^2/4 + 2\delta^2/9}$ and $E_3 = 0$. Since $E_3(k_x = 0, k_y = 0, k_z) = 0$ for any k_z , the $E_2^{(+)}$ and E_3 bands will cross along k_z at zero energy, at $k_z = \pm \sqrt{|E_g| \delta / P_\parallel^2}$.

For $\Delta \gg \delta$, which corresponds well to the studied material ($\Delta = 400$ meV and $\delta = 30$ meV), the above eigenenergies can be expressed as $E_2^+ \approx -2\delta/3$ and $E_2^- \approx -\Delta$. The separation $E_3 - E_2^+ \approx 2\delta/3$ then gives a rough estimate for the energy scale at which the symmetry-protected Dirac electrons appear in Cd_3As_2 (Figs. 3a,b in the main text). In contrast, the Kane electrons exist at a considerably larger energy scale, comparable to the strength of the spin-orbit coupling Δ and thus extend over several hundred meV.

Let us also note that for a negligible anisotropy ($\delta = 0$ and $P_\parallel = P_\perp = P$) and a vanishing band gap ($E_g = 0$), the band structure can be expressed analytically in the limit of infinitely strong ($\Delta \rightarrow \infty$) or vanishing ($\Delta = 0$) spin-orbit coupling. The former case has been considered in Ref. 4. The corresponding band structure comprises the doubly-degenerate flat band $E(k) = 0$ and 3D cones $E(k) = \pm v\hbar|k|$ that host the 3D massless charge carriers with a velocity of $v = \sqrt{2/3}P/\hbar$ referred to as Kane electrons. In the other limit, for the vanishing Δ , we also obtain a doubly spin-degenerate 3D cone $E(k) = \pm v\hbar|k|$, but with a fourfold degenerate flat band $E(k) = 0$ and a velocity given by $v = P/\hbar$.

BODNAR/KANE MODEL – OPTICAL RESPONSE AT ZERO MAGNETIC FIELD

In this part we use the Bodnar model and linear response theory to calculate the real part of optical conductivity at $B = 0$,

$$\text{Re}\{\sigma_{ii}(\omega)\} = \frac{\sigma_0}{\omega} \sum_{l,l'=1}^8 \int \frac{d^3\mathbf{k}}{(2\pi)^3} \underbrace{(f_D(E_l(\mathbf{k})) - f_D(E_{l'}(\mathbf{k})))}_{\text{band occupation}} \underbrace{|c_l^\dagger(\mathbf{k}) \nabla_{k_i} H(\mathbf{k}) c_{l'}(\mathbf{k})|^2}_{\text{interband coupling}} \underbrace{\delta(\hbar\omega - (E_l(\mathbf{k}) - E_{l'}(\mathbf{k})))}_{\Rightarrow \text{joint density of states}} \quad (\text{S7})$$

where $\sigma_0 = \pi e^2/\hbar^2$ and l, l' label the eigenstates of $\hat{H}(\mathbf{k})$ in Eq. (S1). One has the velocity matrix components $\nabla_{k_i} H = P J_i$ where $i = x, y, z$ labels the Cartesian coordinates and where we consider the experimentally relevant case $P_\perp \approx P_\parallel = P$.

Studying the optical response at relatively high energies ($\hbar\omega \gg \delta$), we may set $\delta = 0$. Any eigenstate $|l, \mathbf{k}\rangle$ can then be related, according to Eq. (S6), to a state of momentum along z , $|l, \mathbf{k}\rangle = \hat{U}_\phi^\dagger \hat{U}_\theta^\dagger |l, k_z = |\mathbf{k}|\rangle$, with the corresponding spherical coordinates θ, ϕ .

Furthermore, we take $|E_g| \ll \hbar\omega$ and consider Δ to be sufficiently large so that we project out the states at the energy of $-\Delta$, which are, up to lowest order in Pk/Δ :

$$\begin{pmatrix} 0 \\ 0 \\ \sqrt{2/3} \\ -\sqrt{1/3} \\ 0 \\ 0 \\ 0 \\ 0 \end{pmatrix}, \begin{pmatrix} 0 \\ 0 \\ 0 \\ 0 \\ 0 \\ \sqrt{2/3} \\ -\sqrt{1/3} \end{pmatrix}. \quad (\text{S8})$$

The projected 6×6 Hamiltonian thus reads:

$$\hat{H}_\infty(\mathbf{k}) \equiv (Q \cdot P)^\dagger \hat{H}(Q \cdot P) = \hat{H}_\infty(\mathbf{k} = 0) + P\mathbf{k} \cdot \hat{\mathbf{J}}_\infty \quad (\text{S9})$$

$$= \begin{pmatrix} 0 & 0 & 0 & 0 & 0 & Pk_- \\ 0 & 0 & 0 & Pk_+ & 0 & 0 \\ 0 & 0 & 0 & \sqrt{\frac{2}{3}}Pk_z & 0 & \frac{1}{\sqrt{3}}Pk_+ \\ 0 & Pk_- & \sqrt{\frac{2}{3}}Pk_z & 0 & -\frac{1}{\sqrt{3}}Pk_+ & 0 \\ 0 & 0 & 0 & -\frac{1}{\sqrt{3}}Pk_- & 0 & \sqrt{\frac{2}{3}}Pk_z \\ Pk_+ & 0 & \frac{1}{\sqrt{3}}Pk_- & 0 & \sqrt{\frac{2}{3}}Pk_z & 0 \end{pmatrix}, \quad (\text{S10})$$

where $k_\pm = (k_x \pm ik_y)/\sqrt{2}$ and

$$Q \cdot P = \begin{pmatrix} 0 & 0 & 0 & 1 & 0 & 0 \\ 0 & 1 & 0 & 0 & 0 & 0 \\ 0 & 0 & 0 & 0 & \frac{1}{\sqrt{3}} & 0 \\ 0 & 0 & 0 & 0 & \sqrt{\frac{2}{3}} & 0 \\ 0 & 0 & 0 & 0 & 0 & 1 \\ 1 & 0 & 0 & 0 & 0 & 0 \\ 0 & 0 & \frac{1}{\sqrt{3}} & 0 & 0 & 0 \\ 0 & 0 & \sqrt{\frac{2}{3}} & 0 & 0 & 0 \end{pmatrix}. \quad (\text{S11})$$

We can use the previous rotation property,

$$\begin{aligned} \mathbf{J}_\infty \cdot \mathbf{n} &= J_{\infty,x} \sin(\theta) \cos(\phi) + J_{\infty,y} \sin(\theta) \sin(\phi) + J_{\infty,z} \cos(\theta) = U_{\infty,\phi}^\dagger (J_{\infty,x} \sin(\theta) + J_{\infty,z} \cos(\theta)) U_{\infty,\phi} \\ &= U_{\infty,\phi}^\dagger U_{\infty,\theta}^\dagger J_{\infty,z} U_{\infty,\theta} U_{\infty,\phi} \end{aligned} \quad (\text{S12})$$

$$U_{\infty,\phi} = \text{diag}(e^{2i\phi}, e^{-i\phi}, 1, 1, e^{i\phi}, e^{i\phi}) \quad (\text{S13})$$

$$U_{\infty,\theta} = \exp(i\theta L_\infty) \quad (\text{S14})$$

$$L_\infty = \begin{pmatrix} 0 & 0 & 0 & 0 & i\frac{\sqrt{3}}{2} & 0 \\ 0 & 0 & i\frac{\sqrt{3}}{2} & 0 & 0 & 0 \\ 0 & -i\frac{\sqrt{3}}{2} & 0 & 0 & i & 0 \\ 0 & 0 & 0 & 0 & 0 & \frac{i}{2} \\ -i\frac{\sqrt{3}}{2} & 0 & -i & 0 & 0 & 0 \\ 0 & 0 & 0 & -\frac{i}{2} & 0 & 0 \end{pmatrix}, \quad (\text{S15})$$

and obtain the states $|l, k_z = |\mathbf{k}|\rangle$ from the following rotated Hamiltonian,

$$\hat{H}_{\infty,z}(\mathbf{k}) \equiv U_{\infty,\phi}^\dagger U_{\infty,\theta}^\dagger (Q \cdot P)^\dagger \hat{H}(Q \cdot P) U_{\infty,\theta} U_{\infty,\phi} = \sqrt{\frac{2}{3}} Pk \hat{J}_{\infty,z}. \quad (\text{S16})$$

We find the following three eigenenergies:

$$E_0(\mathbf{k}) = 0, E_{\pm}(\mathbf{k}) = \pm \sqrt{\frac{2}{3}}Pk, \quad (\text{S17})$$

corresponding to the following six eigenstates:

$$\begin{pmatrix} 1 \\ 0 \\ 0 \\ 0 \\ 0 \\ 0 \end{pmatrix}_{0,1}, \begin{pmatrix} 0 \\ 1 \\ 0 \\ 0 \\ 0 \\ 0 \end{pmatrix}_{0,2}, \frac{1}{\sqrt{2}} \begin{pmatrix} 0 \\ 0 \\ 1 \\ 1 \\ 0 \\ 0 \end{pmatrix}_{+,1}, \frac{1}{\sqrt{2}} \begin{pmatrix} 0 \\ 0 \\ 0 \\ 1 \\ 1 \\ 1 \end{pmatrix}_{+,2}, \frac{1}{\sqrt{2}} \begin{pmatrix} 0 \\ 0 \\ 1 \\ -1 \\ 0 \\ 0 \end{pmatrix}_{-,1}, \text{ and } \frac{1}{\sqrt{2}} \begin{pmatrix} 0 \\ 0 \\ 0 \\ 0 \\ 1 \\ -1 \end{pmatrix}_{-,2}. \quad (\text{S18})$$

Since the energies only depend on $|\mathbf{k}|$, the integration over θ, ϕ in Eq.(S7) leads to the following interband coupling for $\sigma_{xx}(\omega)$

$$K_{ll'}^x = P^2 \int d\theta d\phi |\langle l, \mathbf{k} | J_x | l', \mathbf{k} \rangle|^2 = P_{\perp}^2 \int d\theta d\phi |\langle l, k_z = |\mathbf{k}| | \hat{U}_{\theta} \hat{U}_{\phi} J_x \hat{U}_{\phi}^{\dagger} \hat{U}_{\theta}^{\dagger} | l', k_z = |\mathbf{k}| \rangle|^2 \quad (\text{S19})$$

$$= P^2 \int d\theta d\phi |\langle l, k_z = |\mathbf{k}| | \hat{J}_x \cos(\theta) \cos(\phi) - \hat{J}_y \sin(\phi) + \hat{J}_z \sin(\theta) \cos(\phi) | l', k_z = |\mathbf{k}| \rangle|^2 \quad (\text{S20})$$

$$= \frac{4\pi P^2}{3} \left(2|\langle l, k_z = |\mathbf{k}| | \hat{J}_x | l', k_z = |\mathbf{k}| \rangle|^2 + |\langle l, k_z = |\mathbf{k}| | \hat{J}_z | l', k_z = |\mathbf{k}| \rangle|^2 \right), \quad (\text{S21})$$

where the commutators $[\hat{L}, \hat{J}_z] = -i\hat{J}_y$, $[\hat{L}, \hat{J}_y] = 0$ and $[\hat{L}, \hat{J}_x] = i\hat{J}_z$ have been used.

In the basis of eigenstates ordered as in Eq. (S18), and adding the two states at the energy of $-\Delta$ states from Eq.(S8) in the last two columns, the interband coupling matrix is, up to the lowest order in Pk/Δ ,

$$K_{ll'}^x \approx \frac{4\pi P^2}{3} \begin{pmatrix} 0 & 0 & 0 & \frac{1}{2} & 0 & \frac{1}{2} & 0 & 0 \\ 0 & 0 & \frac{1}{2} & 0 & \frac{1}{2} & 0 & 0 & 0 \\ 0 & \frac{1}{2} & \frac{2}{3} & 0 & 0 & \frac{1}{3} & \frac{1}{6} & \frac{1}{3} \\ \frac{1}{2} & 0 & 0 & \frac{2}{3} & \frac{1}{3} & 0 & \frac{1}{3} & \frac{1}{6} \\ 0 & \frac{1}{2} & 0 & \frac{1}{3} & \frac{2}{3} & 0 & \frac{1}{6} & \frac{1}{3} \\ \frac{1}{2} & 0 & \frac{1}{3} & 0 & 0 & \frac{2}{3} & \frac{1}{3} & \frac{1}{6} \\ 0 & 0 & \frac{1}{6} & \frac{1}{3} & \frac{1}{6} & \frac{1}{3} & 0 & 0 \\ 0 & 0 & \frac{1}{3} & \frac{1}{6} & \frac{1}{3} & 0 & 0 & 0 \end{pmatrix}. \quad (\text{S22})$$

Finally, we obtain and approximate formula for the optical conductivity:

$$\text{Re} \{ \sigma_{xx}^{\infty}(\omega > 0) \} \approx \frac{\sigma_0}{\omega} \frac{4\pi P^2}{3} \int \frac{k^2 dk}{(2\pi)^3} \left[\delta \left(\hbar\omega - \sqrt{\frac{2}{3}}Pk \right) + \frac{2}{3} \delta \left(\hbar\omega - 2\sqrt{\frac{2}{3}}Pk \right) + \delta \left(\hbar\omega - \Delta - \sqrt{\frac{2}{3}}Pk \right) \right] \quad (\text{S23})$$

$$\approx \frac{e^2}{4\pi v \hbar} \omega \left[\frac{13}{12} + \theta(\hbar\omega - \Delta) \left(1 - \frac{\Delta}{\hbar\omega} \right)^2 \right], \quad (\text{S24})$$

where we have introduced the velocity $v = \sqrt{2/3}P/\hbar$ of Kane electrons in the second line.

The last term of the above expression for conductivity represents a good approximation for $\Delta \ll Pk = \sqrt{3/2}(\hbar\omega - \Delta)$ and its profile fits our experimental data well: (i) it is linear in ω at low frequencies ($\hbar\omega \ll \Delta$), (ii) it becomes superlinear for $\hbar\omega$ comparable with Δ , (iii) for $\hbar\omega \gg \Delta$ the corresponding slope becomes roughly twice as large as compared to low ω , and (iv) the high frequency part of optical conductivity approaches $\hbar\omega \approx \Delta$ when $\text{Re} \{ \sigma_{xx}^{\infty}(\omega > 0) \}$ is extrapolated to zero. Let us note that the discontinuity in Eq. (S24) is removed when some disorder as well as finite temperature are considered and the step-like Heaviside function is replaced by some smooth profile. Notice further that, to achieve quantitative agreement, a velocity close to half of the value deduced from magneto-optical data has to be considered, see the main text.

We emphasize that the main feature of the change in the slope of the optical conductivity arises, in the form of the step function, due to the presence of novel excitations available at $\hbar\omega \sim \Delta$. Indeed, the lower cone (green in

Fig. 3b,c of the main text) flattens in response to the hybridization with the spin-orbit-split band (yellow) and contributes at these energies to the optical conductivity. This is a pure band effect that yields roughly a factor of 2 to the optical conductivity. Notice, however, that a change in the velocity also affects the optical conductivity via the density of states, which scales as v^{-3} . If we take the Bodnar (or Kane) model literally at high energies, one obtains an asymptotic change in the velocity $\sqrt{2/3}v \rightarrow v$, which would in principle lower the density of states and thus the optical conductivity, such that the effect would be less pronounced there. However, this effect is compensated by non-linear corrections to the band dispersion at energies $\hbar\omega \gg \Delta$. These corrections generically lower the band velocity rather than enhance it because the involved wave vectors approach the Brillouin-zone borders. The resulting superlinear behavior in the optical conductivity is clearly visible in the inset of Fig. 1(b) in the main text, in the 0.5...1.5 eV range. This effect is not included in the present models that arise from a $k \cdot p$ theory in the vicinity of the Γ point. We therefore attribute the slope change in the optical conductivity mainly to the above-mentioned accessibility of novel electronic excitations.

BODNAR MODEL – LANDAU LEVEL SPECTRUM

Here we calculate the Landau level spectrum within the Bodnar model, following the approach of Wallace [5]. Experimentally, we probe the system at relatively high energies, well above the Lifshitz point, where the whole band structure is fairly isotropic and the spectrum depends only weakly on the direction of the magnetic field. Therefore, we only consider the magnetic field applied along the tetragonal [001] axis in our below presented analytical calculations. For the other experimentally explored [112] direction, we show results of numerical calculations only (Fig. S1b).

We employ the standard Peierls substitution $\mathbf{k} \rightarrow \mathbf{k} - e\mathbf{A}/\hbar$ in the Hamiltonian Eq.(S1) and search for eigenstates in the form

$$\phi_n = \left(\alpha_{1,+}\phi_n \quad \alpha_{2,+}\phi_{n+1} \quad \alpha_{3,+}\phi_{n-1} \quad \alpha_{4,+}\phi_{n-1} \quad \alpha_{1,-}\phi_{n-1} \quad \alpha_{2,-}\phi_{n-2} \quad \alpha_{3,-}\phi_n \quad \alpha_{4,-}\phi_n \right), \quad (\text{S25})$$

where $\phi_n = \phi_n(y + p_x l_B^2) e^{ip_x x}$ are the solutions of the harmonic oscillator, and $l_B = \sqrt{\hbar/eB}$ is the magnetic length.

The coefficients are solutions of the following eigenvalue equation:

$$\hat{H}_B \Psi = E \Psi,$$

with $\Psi = (\alpha_{1,+}, \alpha_{2,+}, \alpha_{3,+}, \alpha_{4,+}, \alpha_{1,-}, \alpha_{2,-}, \alpha_{3,-}, \alpha_{4,-})$ and

$$\hat{H}_B = \begin{pmatrix} E_g & \sqrt{n+1} \frac{P_{\perp}}{l_B} & -\sqrt{n} \frac{P_{\perp}}{l_B} & 0 & 0 & 0 & 0 & P_{\parallel} k_z \\ \sqrt{n+1} \frac{P_{\perp}}{l_B} & 0 & 0 & 0 & 0 & 0 & 0 & 0 \\ -\sqrt{n} \frac{P_{\perp}}{l_B} & 0 & -\frac{2}{3} \Delta & \frac{\sqrt{2}\Delta}{3} & 0 & 0 & 0 & 0 \\ 0 & 0 & \frac{\sqrt{2}\Delta}{3} & -(\delta + \frac{\Delta}{3}) & P_{\parallel} k_z & 0 & 0 & 0 \\ 0 & 0 & 0 & P_{\parallel} k_z & E_g & \sqrt{n-1} \frac{P_{\perp}}{l_B} & \sqrt{n} \frac{P_{\perp}}{l_B} & 0 \\ 0 & 0 & 0 & 0 & \sqrt{n-1} \frac{P_{\perp}}{l_B} & 0 & 0 & 0 \\ 0 & 0 & 0 & 0 & \sqrt{n} \frac{P_{\perp}}{l_B} & 0 & -\frac{2}{3} \Delta & \frac{\sqrt{2}\Delta}{3} \\ P_{\parallel} k_z & 0 & 0 & 0 & 0 & 0 & \frac{\sqrt{2}\Delta}{3} & -(\delta + \frac{\Delta}{3}) \end{pmatrix} \quad (\text{S26})$$

the eigenvalues of which are the searched Landau levels.

Since we are interested in sharp spectral features in the magneto-optical response, we now focus on $k_z = 0$, which is the relevant case for Kane/Bodnar electrons at energies well above the Lifshitz point.

In this limit, all Landau levels of Bodnar/Kane electrons, including the fundamental one $n = 1$, become 1D bands dispersing with k_z and implying extrema at $k_z = 0$. These extrema give rise to characteristic singularities in the (joint) density of states, and therefore, to a strongly enhanced response in our magneto-optical measurements. This is in contrast with the fundamental ($n = 0$) levels of 3D Dirac electrons. These levels disperse *linearly* with k_z and for the fundamental CR mode ($n = 0^- \rightarrow 1$ and $n = 0^+ \rightarrow 1$, see Fig. 4a of the main text) imply rather flat density of states. This yields an essentially featureless magneto-optical response, apart from the low-energy cut-off due to the non-zero Fermi level, which is discussed in the next section.

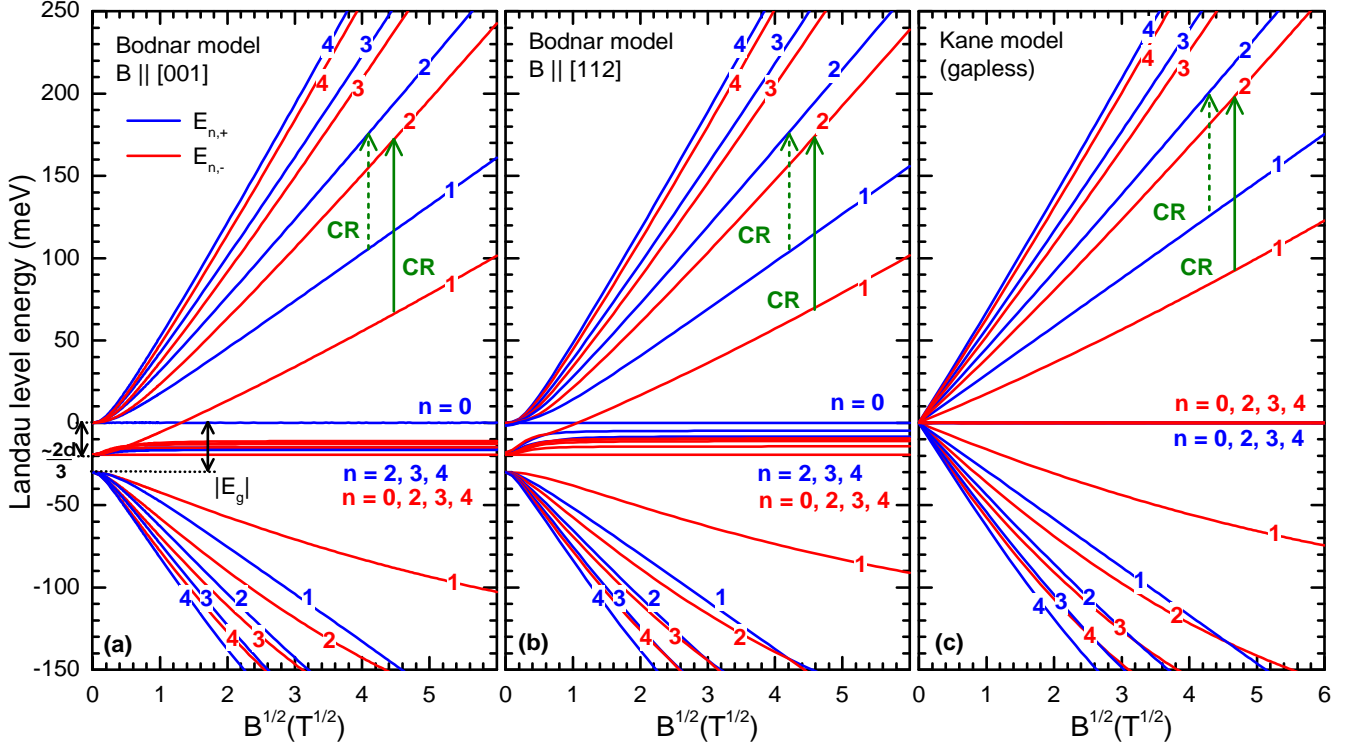


Fig. S1. (a): The LL spectrum (at $k_z = 0$) calculated using the Bodnar model for $\delta = 30$ meV, $E_g = -30$ meV and magnetic field oriented along the [001] direction. (b): The LL spectrum (at $k_{112} = 0$) calculated using the Bodnar model for $\delta = 30$ meV, $E_g = -30$ meV and magnetic field oriented along the [112] direction. (c): The isotropic LL spectrum (at $k = 0$) calculated within the Kane model for $\delta = E_g = 0$. The spin-orbit coupling $\Delta = 400$ meV and the velocity parameter $v = 0.93 \times 10^6$ m/s were used in all the cases. Only LLs at low energies and with indices $n = 0 \dots 4$ were plotted. The blue and red curves correspond to the spin down $E_{n,-}$ and spin up $E_{n,+}$ levels, respectively, see the text. The color coding in the part (b) was chosen to reflect the spin projection in high fields (corresponding to the Kane model). At low energies, spin up and down states are strongly mixed for $B \parallel [112]$. The full vertical arrows correspond to CR modes active when the quantum limit is approached, cf. Fig. 4b in the main text. Notably, the LL spectra calculated within the Bodnar and Kane model become nearly identical for energies high enough, which implies practically the same CR energies. The $n = 0$ and $n = 1$ LLs in the Bodnar model (a) and (b), which cross at the magnetic-field of $B_c \approx 2$ and 1 T, respectively, play the role of zero-mode levels within the Dirac picture ($n = 0^+$ and $n = 0^-$ in Fig. 4a of the main text). At $B < B_c$, these two levels cross as a function of the momentum k along the field direction at the corresponding Dirac points.

For $k_z = 0$, the two \pm subspaces are decoupled, and one can search for solutions of the form ($n \geq 0$)

$$\Psi_{n,+} = \begin{pmatrix} \alpha_{1,+} \phi_{n-1} & \alpha_{2,+} \phi_n & \alpha_{3,+} \phi_{n-2} & \alpha_{4,+} \phi_{n-2} & 0 & 0 & 0 & 0 \end{pmatrix}, \quad (\text{S27})$$

$$\Psi_{n,-} = \begin{pmatrix} 0 & 0 & 0 & 0 & \alpha_{1,-} \phi_{n-1} & \alpha_{2,-} \phi_{n-2} & \alpha_{3,-} \phi_n & \alpha_{4,-} \phi_n \end{pmatrix}. \quad (\text{S28})$$

If $n \geq 2$ the coefficients are solution of

$$\begin{pmatrix} E_g & \sqrt{n} \frac{P_{\perp}}{l_B} & -\sqrt{n-1} \frac{P_{\perp}}{l_B} & 0 \\ \sqrt{n} \frac{P_{\perp}}{l_B} & 0 & 0 & 0 \\ -\sqrt{n-1} \frac{P_{\perp}}{l_B} & 0 & -\frac{2}{3} \Delta & \frac{\sqrt{2}\Delta}{3} \\ 0 & 0 & \frac{\sqrt{2}\Delta}{3} & -(\delta + \frac{\Delta}{3}) \end{pmatrix} \begin{pmatrix} \alpha_{1,+} \\ \alpha_{2,+} \\ \alpha_{3,+} \\ \alpha_{4,+} \end{pmatrix} = E_{n,+} \begin{pmatrix} \alpha_{1,+} \\ \alpha_{2,+} \\ \alpha_{3,+} \\ \alpha_{4,+} \end{pmatrix} \quad (\text{S29})$$

$$\begin{pmatrix} E_g & \sqrt{n-1} \frac{P_{\perp}}{l_B} & \sqrt{n} \frac{P_{\perp}}{l_B} & 0 \\ \sqrt{n-1} \frac{P_{\perp}}{l_B} & 0 & 0 & 0 \\ \sqrt{n} \frac{P_{\perp}}{l_B} & 0 & -\frac{2}{3} \Delta & \frac{\sqrt{2}\Delta}{3} \\ 0 & 0 & \frac{\sqrt{2}\Delta}{3} & -(\delta + \frac{\Delta}{3}) \end{pmatrix} \begin{pmatrix} \alpha_{1,-} \\ \alpha_{2,-} \\ \alpha_{3,-} \\ \alpha_{4,-} \end{pmatrix} = E_{n,-} \begin{pmatrix} \alpha_{1,-} \\ \alpha_{2,-} \\ \alpha_{3,-} \\ \alpha_{4,-} \end{pmatrix}. \quad (\text{S30})$$

The lowest Landau levels $n = 0$ and $n = 1$ are special in that many components simply vanish,

1. For $n = 0$, the wave functions have the form

$$\phi_{0,+} = (0 \ \phi_0 \ 0 \ 0 \ 0 \ 0 \ 0 \ 0), \quad (\text{S31})$$

$$\phi_{0,-} = (0 \ 0 \ 0 \ 0 \ 0 \ 0 \ \alpha_{3,-}\phi_0 \ \alpha_{4,-}\phi_0). \quad (\text{S32})$$

The three corresponding eigenenergies are

$$E_{0,+} = 0, \quad (\text{S33})$$

$$E_{0,-}^{(\pm)} = -\frac{\Delta + \delta}{2} \pm \sqrt{\left(\frac{\Delta - \delta/3}{2}\right)^2 + 2\delta^2/9}. \quad (\text{S34})$$

The “−” coefficients are the solution of

$$\begin{pmatrix} -\frac{2}{3}\Delta & \frac{\sqrt{2}\Delta}{3} \\ \frac{\sqrt{2}\Delta}{3} & -(\delta + \frac{\Delta}{3}) \end{pmatrix} \begin{pmatrix} \alpha_{2,-} \\ \alpha_{4,-} \end{pmatrix} = E_{0,-}^{(\pm)} \begin{pmatrix} \alpha_{2,-} \\ \alpha_{4,-} \end{pmatrix}. \quad (\text{S35})$$

2. For $n = 1$, the wave functions have the form

$$\phi_{1,+} = (\alpha_{1,+}\phi_0 \ \alpha_{2,+}\phi_1 \ 0 \ 0 \ 0 \ 0 \ 0 \ 0), \quad (\text{S36})$$

$$\phi_{1,-} = (0 \ 0 \ 0 \ 0 \ \alpha_{1,-}\phi_0 \ 0 \ \alpha_{3,-}\phi_1 \ \alpha_{4,-}\phi_1). \quad (\text{S37})$$

The two “+” eigenenergies are

$$E_{1,+}^{(\pm)} = \frac{E_g}{2} \pm \sqrt{\left(\frac{E_g}{2}\right)^2 + \left(\frac{P_{\perp}}{l_B}\right)^2}, \quad (\text{S38})$$

and the “+” coefficients are solutions of

$$\begin{pmatrix} E_g & \frac{P_{\perp}}{l_B} \\ \frac{P_{\perp}}{l_B} & 0 \end{pmatrix} \begin{pmatrix} \alpha_{1,+} \\ \alpha_{2,+} \end{pmatrix} = E_{1,+}^{(\pm)} \begin{pmatrix} \alpha_{1,+} \\ \alpha_{2,+} \end{pmatrix}. \quad (\text{S39})$$

The three “−” eigenenergies are the solution of the following 3×3 matrix equation

$$\begin{pmatrix} E_g & \frac{P_{\perp}}{l_B} & 0 \\ \frac{P_{\perp}}{l_B} & -\frac{2}{3}\Delta & \frac{\sqrt{2}\Delta}{3} \\ 0 & \frac{\sqrt{2}\Delta}{3} & -(\delta + \frac{\Delta}{3}) \end{pmatrix} \begin{pmatrix} \alpha_{1,-} \\ \alpha_{2,-} \\ \alpha_{4,-} \end{pmatrix} = E_{1,-} \begin{pmatrix} \alpha_{1,-} \\ \alpha_{2,-} \\ \alpha_{4,-} \end{pmatrix}. \quad (\text{S40})$$

The LL spectrum calculated within the Bodnar model has been plotted for $B \parallel [001] \parallel z$ and for $B \parallel [112]$ into Figs. [S1a](#) and [S1b](#), respectively, for parameters considered in the main text ($v = 0.93 \times 10^6$ m/s, $\Delta = 400$ meV, $\delta = 30$ meV and $E_g = -30$ meV). The latter set of LLs was obtained by the full numerical diagonalization of the corresponding 8×8 Hamiltonian assuming momentum $k_{112} = 0$. In this case, the form of the Hamiltonian does not allow us to facilitate the solution by its separation into two independent 4×4 Hamiltonians as in the $[001]$ case. The color coding of the spin-up and down projections in Figs. [S1b](#) reflects only the approximate spin projection in the limit of high magnetic fields and high energies, when the Bodnar model becomes equivalent to the gapless Kane model. The LL spectrum calculated within the Bodnar model is compared to LLs of gapless Kane electrons ($\delta = E_g = 0$) in Fig. [S1c](#). In all three cases, the fundamental CR mode observed in high magnetic fields is identified as the excitation from $n = 1$ to $n = 2$ LL of the $E_{n,-}$ series and marked by the full vertical arrow. This is because the Fermi energy remains in an electron-doped system pinned to the bottom of the $n = 1$ LL of the $E_{n,-}$ series when the quantum limits is achieved. In high fields, the fundamental CR mode fairly well follows the \sqrt{B} dependence.

Let us now discuss in a greater detail the Landau levels ($n = 0$ and $n = 1$ from the $E_{n,+}$ and $E_{n,-}$ series, respectively), which clearly cross at $B_c \approx 2$ and 1 T in Figs. [S1a](#) and [S1b](#), respectively. This crossing is a direct consequence of the band inversion, present in the Bodnar model when $E_g < 0$, and it is also typical of other materials with an inverted band structure, for instance, of topological insulators [\[6\]](#). The significance of these two crossing levels becomes clear when we look at their particular dispersions with the momentum k along the magnetic field. At $B < B_c$, these

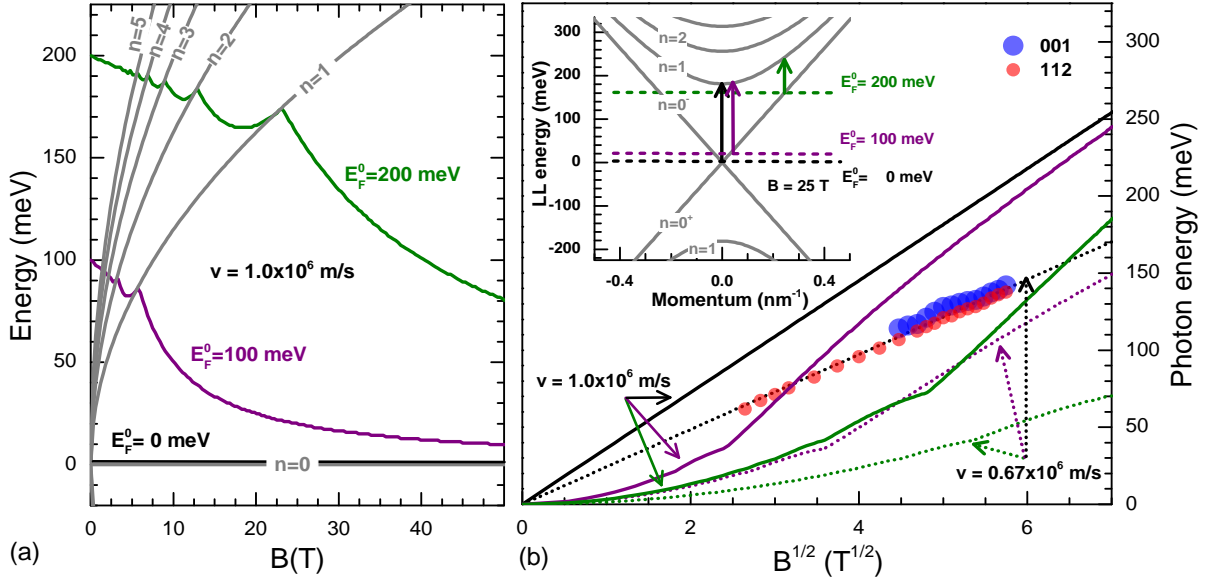


Fig. S2. Part (a): The Fermi energy in a system with 3D massless Dirac fermions ($v = 1.00 \times 10^6$ m/s) as a function of B for the constant carrier density, given by the zero-field Fermi levels: $E_F^0 = 0, 100$ and 200 meV. The Landau level energies, $E_n(k=0)$ for $n = 0 \dots 5$, have been plotted for comparison. Part (b): The numerically calculated field dependence of the low-energy absorption edge $L_{0 \rightarrow 1}$ in a system with Landau-quantized 3D Dirac electrons with the fixed carrier concentrations (i.e., field-dependent E_F). We have considered two different velocity parameters, $v = 1.00 \times 10^6$ m/s and $v = 0.67 \times 10^6$ m/s (full and dotted lines, respectively), and three different values of the zero-field Fermi energy, $E_F^0 = 0, 100$ and 200 meV (black, violet and green, respectively). The full circles are energies of the experimentally observed fundamental CR modes in the two investigated samples. The inset shows the position of the Fermi energies $E_F(B)$ within the LL spectrum of 3D Dirac electrons at $B = 25$ T, assuming $v = 1.00 \times 10^6$ m/s and three different zero-field chemical potentials E_F^0 . The vertical arrows mark the excitations corresponding to the low-energy absorption edge $L_{0 \rightarrow 1}$. The experimentally observed (fundamental) CR modes with a clear \sqrt{B} dependence could be, within the picture of 3D massless Dirac electrons, explained only for a vanishing Fermi level (and the velocity 0.67×10^6 m/s). As we show in the text below, this is at odds with our estimates for the Fermi energy $E_F^{001} \sim 200$ meV and $E_F^{112} \sim 100$ meV for the (001) and (112)-oriented samples, respectively. These estimates are based on the onsets of interband optical absorption (Fig. 1b of the main text) and on the plasma edge splitting at low magnetic fields (Fig. S4).

dispersions imply their crossing in the momentum space for a certain non-zero momentum $k \lesssim k^D$ (and symmetrically for $-k$). At low fields, these specific levels thus play the role of the zero-mode levels of Dirac electrons in Cd_3As_2 . Within the Dirac picture, these zero-mode LLs (denoted as $n = 0^+$ and $n = 0^-$ in Fig. 4a of the main text) disperse linearly in the vicinity of the Dirac nodes. At magnetic fields above $B > B_c$, the low-energy spectrum loses the character of Dirac-like Landau levels and there a real band gap opens between $n = 0$ and $n = 1$ levels, which is typical of Kane electrons.

The dipole selection rules for inter-LL transitions (at $k_z = 0$) are obtained by evaluating the matrix elements of $\hat{J}_\pm = \hat{J}_x \pm i\hat{J}_y$. In the Faraday configuration (i.e., for radiation propagating along the magnetic field) we obtain:

1. $\Psi_n \rightarrow \Psi_{n\pm 1}$,
2. transitions between $\Psi_{n,-}$ and $\Psi_{m,+}$ states (so-called spin-flip transitions) are forbidden.

3D DIRAC ELECTRONS IN THE QUANTUM LIMIT – OPTICAL RESPONSE

In the main text, based on purely qualitative arguments, we have excluded that the 3D Dirac electrons in Cd_3As_2 could be responsible for the specific optical response of Cd_3As_2 in high magnetic fields. Here, we extend our considerations and present a quantitative comparison of our cyclotron resonance (CR) data with the response theoretically expected for Landau-quantized 3D Dirac electrons.

Let us first summarize our basic experimental findings. The collected optical and magneto-optical data clearly show the presence of 3D massless charge carriers in Cd_3As_2 and indicate high isotropy of the corresponding conical band structure. The zero-field data (onsets of interband absorption and the ratio of plasma energies) provide us with the basic estimates for the Fermi energies $E_F^0 = 50 - 100$ meV and $100 - 200$ meV, for the (112)-oriented and (001)-oriented Cd_3As_2 samples, respectively. The lower bound is obtained assuming ideal 3D Dirac cones without any electron-hole asymmetry. The real values of E_F most likely approach the upper bound of the above intervals.

The application of high magnetic fields allowed us to observe fundamental CR modes of massless particles in both of the samples. The fundamental CR mode here denotes the situation when electrons are excited from the lowest electronic Landau level (in the conduction band). Let us now (hypothetically) assume that we are indeed dealing with 3D massless Dirac electrons and compare the theoretically expected response with our experimental data.

In the LL spectrum of 3D massless Dirac electrons, $E_n = \pm v\sqrt{2e\hbar Bn + \hbar^2 k^2}$, the fundamental CR mode of electrons corresponds to the excitations from the two $n = 0$ levels to the upper $n = 1$ level, see Fig. 4a in the main text. This fundamental CR mode of 3D Dirac electrons does not imply any singularity in the joint density of states and its only characteristic spectral feature is the low-energy absorption edge at $L_{0 \rightarrow 1} = \sqrt{v^2 2e\hbar B + E_F^2} - E_F$.

The non-zero Fermi energy implies that this low energy edge cannot follow the \sqrt{B} dependence, and also becomes sensitive to the particular concentration of charge carriers (cf. an analogous situation for Weyl electrons discussed in Ref. 7). Since this behavior is not seen in high-field CR data, we have concluded in the main text that 3D Dirac electrons cannot be responsible for the observed magneto-optical response.

Nevertheless, for the Fermi energy E_F^0 small enough, the low-energy edge $L_{0 \rightarrow 1}$ still approaches the \sqrt{B} dependence in the limit of high magnetic fields. Moreover, the carrier concentration stays (most likely) constant with the applied magnetic field, which leads to a continuous drop of E_F with B , bringing $L_{0 \rightarrow 1}$ even closer to the \sqrt{B} dependence. Therefore, to support our main conclusions, here we present a quantitative comparison of our CR data with the theoretically expected edge energy $L_{0 \rightarrow 1}$, plotted for realistic v and E_F parameters, see Fig. S2.

Let us first focus on the field dependence of E_F , under the reasonable assumption that the total electron concentration N_{total} does not vary with the magnetic field. Such a dependence has been calculated numerically and plotted in Fig. S2a for three selected values of the zero-field Fermi energies $E_F^0 = 0, 100$ and 200 meV, covering thus the range of the Fermi energies relevant for our samples. The velocity parameter was fixed at $v = 1.00 \times 10^6$ m/s. We see that $E_F(B)$ remains roughly constant below the quantum limit, when $E_1(k=0) < E_F(B)$. Once the quantum limit is achieved, the $E_F(B)$ follows $E_F(B) = N_{\text{total}} v \pi^2 \hbar^2 / (eB)$.

The expected field-dependence of $L_{0 \rightarrow 1}$ has been plotted in Fig. S2b. To illustrate that the low-energy edge $L_{0 \rightarrow 1}$ cannot be used to fit the experimental data by varying the velocity parameter v , we have considered its two different values: $v = 1.00 \times 10^6$ m/s and $v = 0.67 \times 10^6$ m/s (full and dotted lines). The former value was chosen to bring the $L_{0 \rightarrow 1}$ energies close to the experimentally deduced CR energies. The latter value was set to reproduce our experimental data assuming $E_F \equiv 0$ (i.e., $L_{0 \rightarrow 1} = v\sqrt{2e\hbar B}$). As one may expect, the $L_{0 \rightarrow 1}$ energy increases with the velocity parameter, but the \sqrt{B} dependence is not recovered for neither of considered velocities, when the experimental estimates of the zero-field Fermi energies are taken into account. Here we recall our realistic estimates of the zero-field Fermi energies in our samples: $E_F^0 \lesssim 100$ meV and $E_F^0 \approx 200$ meV for our (112)- and (001)-oriented samples, respectively, based on our analysis of the zero-field data (Fig. 1a,b in the main text) and also the low-field plasma-edge splitting described below.

This allows us to exclude that the observed response in our high-field magneto-reflectivity measurements could arise from 3D Dirac electrons in Cd_3As_2 .

BODNAR VERSUS KANE MODEL – COMPARISON

As mentioned in the main text, the tetragonal nature of Cd_3As_2 does not allow the Kane model to be valid down to arbitrarily low energies. Comparing the experimentally observed CR response with the full Bodnar model (Fig. S3) provides us with rough estimates (upper limits) for δ and E_g , which are missing in the simplest gapless Kane model. Convincing agreement between the full Bodnar model and our experimental data (full/open circles versus solid lines in Fig. S3) is obtained when these parameters are taken as large as $E_g = -30$ meV and $\delta = 30$ meV. Let us also note that the origin of the onset $2\delta/3$ appearing for the upper theoretical curve is clarified when confronted with the Landau level spectrum calculated within the full Bodnar model, see Fig. S1a,b.

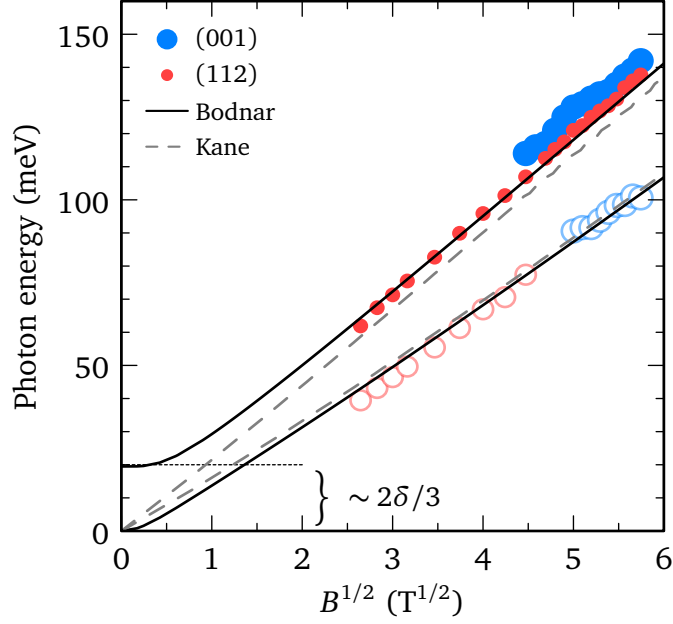


Fig. S3. The experimentally deduced positions of the dominant (full circles) and satellite (open circles) CR modes for both investigated samples. The solid lines show positions expected theoretically within the Bodnar model, assuming $v = 0.93 \times 10^6$ m/s, $\Delta = 400$ meV, $\delta = 30$ meV and $E_g = -30$ meV. The origin of the onset of $2\delta/3$ is explained in the text. For comparison, the dashed lines correspond to the positions of resonances expected within the simplest gapless Kane model (i.e., taking the same parameters, but $\delta = E_g = 0$).

ANISOTROPY OF VELOCITY – A BASIC ESTIMATE

To quantify the anisotropy of Cd_3As_2 based on our magneto-optical data, let us first consider a quasi-classical motion of a charge carrier in a 3D asymmetric conical band. When the magnetic field B is applied, such a particle undergoes a periodic (so-called cyclotron) motion within the plane oriented perpendicular to the field direction. In both momentum and real space, this motion follows an elliptic trajectory characterized by the main axis momenta ($p_\alpha > p_\beta$) and the main axis lengths ($r_\alpha < r_\beta$), respectively. These are connected through relations: $p_\alpha = eBr_\beta$ and $p_\beta = eBr_\alpha$. In addition, the ellipticity of the trajectory may be expressed using the main axes velocities $p_\alpha/p_\beta = v_\alpha/v_\beta$. They correspond to the minimal and maximal in-plane velocities, v_β and v_α , respectively, achieved by the charge carrier during the cyclotron motion.

When the magnetic field is strong enough, only selected trajectories (Landau levels) become quantum-mechanically allowed. This quantization may be described using the semi-classical Bohr-Sommerfeld rule: $\Phi = BS = (n + \xi)\Phi_0$. While following the cyclotron trajectory, the charge carrier encircles an area, $S = \pi r_\alpha r_\beta$, with a total magnetic flux given by an integer (n) multiple of the flux quantum $\Phi_0 = h/e$, corrected by a constant geometrical factor ξ . This latter parameter is specific for a given band profile. For a conical band described by the Weyl or Dirac Hamiltonian, it equals zero, but may reach any value between 0 and 1/2 for an arbitrary band [8–10].

Using this Bohr-Sommerfeld rule, we find the energies of Landau levels within an anisotropic conical band,

$$E_n = \pm \sqrt{v_\alpha v_\beta 2e\hbar B(n + \xi) + v_\gamma^2 \hbar^2 k^2}, \quad (\text{S41})$$

where v_γ stands for the velocity along the direction of the magnetic field. Even though the details of the LL spectrum depend on the specific value of ξ and on the particular spin-splitting of levels, we may conclude that for $k = 0$ the energies of all LLs and all inter-LL excitations become proportional to the geometrical average of the main axis velocities $\sqrt{v_\alpha v_\beta}$.

The tetragonal symmetry, characteristic of Cd_3As_2 and crucial for the presence symmetry-protected 3D Dirac cones at low energies, primarily enters the Bodnar model via crystal field splitting δ . In addition, it may also give rise to an anisotropy of the in-plane and out-of-plane interband matrix element $P_\parallel \neq P_\perp$. Well above the Lifshitz point

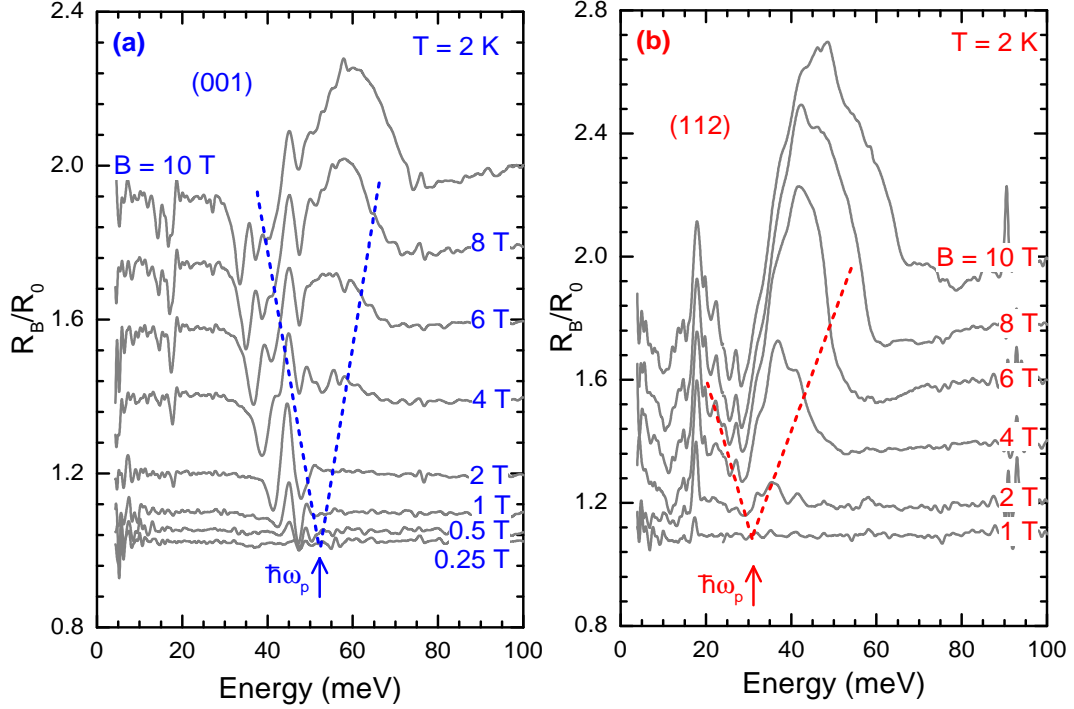


Fig. S4. The splitting of the plasma edge at low magnetic fields as seen in the relative magneto-reflectivity spectra of (001) and (112) sample in the part (a) and (b), respectively. The position of the upper and lower branch is roughly shown by the dashed lines. The sharp features in the spectra are likely due to a thin depletion layer on the surface of samples, see Ref. 12.

in Cd_3As_2 , i.e., for energies $\Delta \gg |E(k)| \gg \delta$, the Kane electron anisotropy is determined mainly by the interband coupling constants. These can be conveniently expressed using in-plane and out-of-plane velocities, $v_{\parallel} = \sqrt{2/3}P_{\parallel}/\hbar$ and $v_{\perp} = \sqrt{2/3}P_{\perp}/\hbar$. A rough estimate for the ratio of these velocities, v_{\perp}/v_{\parallel} , can be obtained from the fairly small, but still present, difference in the energies of the fundamental CR modes, $\alpha = \omega_c^{001}/\omega_c^{112} \sim 1.03$, obtained on samples with the (001)- and (112)-oriented facets. Both these modes evolve with a nearly perfect \sqrt{B} and thus correspond to inter-LL excitations at $k = 0$, which makes them proportional to the geometrical average of the main axis velocities, following Eq. S41.

For the (001)-oriented sample, with the cyclotron motion within an isotropic plane, the CR energy scales linearly with the in-plane velocity, $\omega_c^{001} \propto \sqrt{v_{\parallel}v_{\perp}} = v_{\parallel}$. A more complex result is obtained for the (112)-oriented sample, since the (112)-plane is not isotropic. Assuming that the lattice constants satisfy $a = b = c/2$ (practically fulfilled in Cd_3As_2 [11]), the (112) crystallographic direction becomes equivalent to (1,1,1) direction in the momentum space. The corresponding main axis velocities, in the plane perpendicular to the magnetic field, read v_{\parallel} and $\sqrt{(v_{\parallel}^2 + 2v_{\perp}^2)/3}$, which implies $\omega_c^{112} \propto \sqrt[4]{v_{\parallel}^2(v_{\parallel}^2 + 2v_{\perp}^2)/3}$.

The above formula allows us to express the velocity ratio v_{\perp}/v_{\parallel} using only the experimentally determined parameter $\alpha = 1.03$,

$$\frac{v_{\perp}}{v_{\parallel}} = \sqrt{\frac{13 - \alpha^4}{2\alpha^4}} \approx 0.9.$$

SPLITTING OF PLASMA EDGE AT LOW MAGNETIC FIELDS

The plasma edge in reflectance spectra is characteristic of solids with a non-zero charge carrier density and becomes profoundly modified when a strong enough magnetic field is applied. At relatively low magnetic fields, when the

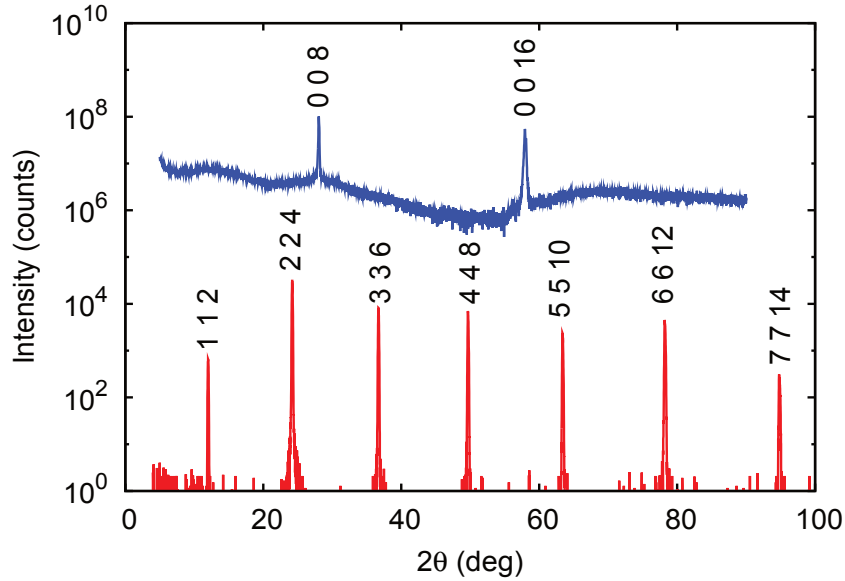


Fig. S5. Symmetric x-ray diffraction scans taken on the (001)- and (112)-oriented samples (top and bottom curve, respectively). The observed Bragg reflections indexed according to the Cd_3As_2 crystal structure reported in Ref. 11 are in agreement with the anticipated surface orientations of the respective samples.

motion of charge carriers is still described by laws of classical mechanics ($\omega_c\tau \lesssim 1$), the standard magneto-plasma theory [13] implies that the plasma edge splits into two branches separated by the cyclotron energy, $\hbar\omega_c = eB/m$. In systems with massless charge carriers, the cyclotron mass increases linearly with the Fermi energy, $m = E_F/v^2$.

The field-induced splitting of the plasma edge has been observed in the response of both investigated Cd_3As_2 samples, see Fig. S4, where the relative magneto-reflectivity spectra have been plotted at low magnetic fields ($B \leq 10$ T). The position of the upper and lower branches of the split plasma edge are approximately shown by dashed lines, which allow us to set rough estimate for the cyclotron energy in our samples. Notably, the observed splitting is significantly higher for the (112)-oriented sample, which is significantly less doped as compared to the (001)-oriented sample and reflects thus the effective cyclotron mass increasing with the carrier concentration.

In numbers, the splitting of the plasma edge in the (001)-oriented and (112)-oriented sample is estimated to ~ 3 and ~ 5 meV/T, which implies the effective mass of $m_{001} \approx 0.04m_0$ and $0.025m_0$, respectively. These values are in rather good agreement with the cyclotron masses $m_{001} = E_F^{001}/v^2 = 0.04m_0$ and $m_{112} = E_F^{112}/v^2 = 0.02m_0$ expected when the parameters deduced from our other optical and magneto-optical data are considered: $v \approx 0.93 \times 10^6$ m/s, $E_F^{001} \approx 200$ meV and $E_F^{112} \approx 100$ meV.

However, we emphasize that the presented estimate of the effective masses is very rough. More precise analysis of the plasma edge splitting is challenging due to an additional series of fairly sharp resonances in the magneto-reflectivity spectra. These are in particular strong in the response of the (001)-oriented sample, see Fig. S4a. Such features have been observed in previous (low-field) magneto-reflectivity experiments performed on Cd_3As_2 [12] and interpreted as the response of a thin depletion layer on the surface. Their appearance in the magneto-reflectivity spectra correlates with the fine structure of the zero-field plasma edge, see Fig. 1a in the main text, present around the energy of 35 and 50 meV in the spectra of the (112)- and (001)-oriented samples, respectively.

SAMPLE SURFACE ORIENTATION

The surface orientations of the two reported Cd_3As_2 samples were confirmed using the x-ray diffraction (XRD). We measured symmetric XRD scans, where the scattering vector is parallel to the sample surface normal and, thus, the lattice planes parallel to the sample surface are probed. Resulting diffractograms are shown in Fig. S5 for both samples. The measured Bragg reflections were indexed according to the crystal structure reported in Ref. 11. Reflection series

$hh2 \cdot h$ and $004 \cdot l$ observed for the (112)- and (001)-oriented samples, respectively, uniquely confirm the orientation of the sample surface facets.

MAGNETO-REFLECTIVITY SPECTRA – ADDITIONAL DATA AND ANALYSIS

As discussed in the main text, the dominant CR mode observed in the magneto-reflectivity response of both studied Cd_3As_2 samples is likely accompanied by a weak satellite CR line at lower photon energies (Fig. 3 of the main text). Here we provide additional data from the (112)-oriented sample and the detailed data analysis of the high-field data taken on the (001)-oriented sample to support the existence of this satellite line.

In the response of the (112)-oriented sample, the satellite line is observed at relatively low magnetic fields. This allows us to identify this CR mode also in low-field data obtained on this sample. These were collected using a superconducting coil and are characterized by a significantly lower noise level. In Fig. S6, we show both low- and high-field spectra (the latter are shown in the main text) in a form of false color plots. The satellite line, $n = 1^\downarrow \rightarrow 2^\downarrow$, is very visible at ~ 9 T, slightly below its theoretical position as calculated using the Bodnar model (dashed line).

However, let us stress that the purpose of these color plots is to show the existence the spectral feature associated with the satellite line, not to show its exact position. These positions are in the magneto-reflectivity experiments not related to particular minima or maxima in R_B/R_0 curves, but instead, they are associated with the corresponding points of inflections in the spectra. Naturally, the points of inflection are not clearly seen in this type of plots. We also note that different color scales used for low- and high-field data in Fig. S6.

The satellite line $n = 1^\downarrow \rightarrow 2^\downarrow$ was observed also in the response of the (001)-oriented sample. Nevertheless, due to a higher electron density, it emerges only in high magnetic fields for which no data from a superconducting coil (with a reduced noise) are available. The position of this satellite line was extracted using procedure visualized in Fig. S7 for three selected magneto-reflectivity spectra. The high-field R_B/R_0 curves (grey circles) were fitted using a high-order polynomial (red curves). The energies of the resonances, associated with the corresponding points of inflections, were then read as the corresponding minima in the first derivative of the polynomial fit (blue curves).

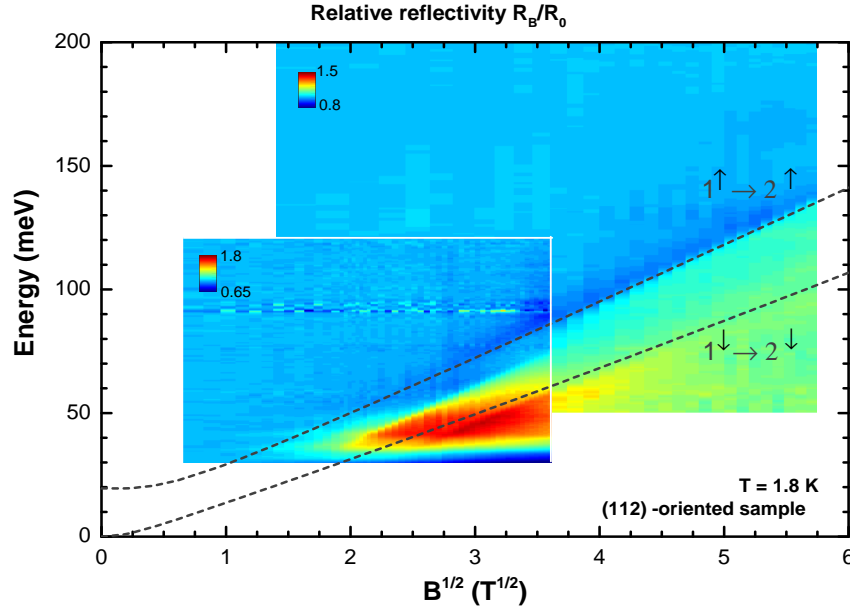


Fig. S6. False color plots of relative magneto-reflectivity R_B/R_0 measured on the (112)-oriented sample at low and high magnetic fields, using superconducting ($B \leq 13$ T) and resistive ($B \leq 33$ T) coils, respectively. The dashed lines correspond to the theoretical positions of $n = 1^\downarrow \rightarrow 2^\downarrow$ and $n = 1^\uparrow \rightarrow 2^\uparrow$ resonances, predicted using Bodnar model with parameters considered in the main text: $v = 0.93 \times 10^6$ m/s, $E_g = -30$ meV, $\delta = 30$ meV and $\Delta = 400$ meV. Note the different energy scale used for the low- and high-field data. The weak satellite line ($n = 1^\downarrow \rightarrow 2^\downarrow$ resonance) is visible slightly below the theoretical curves.

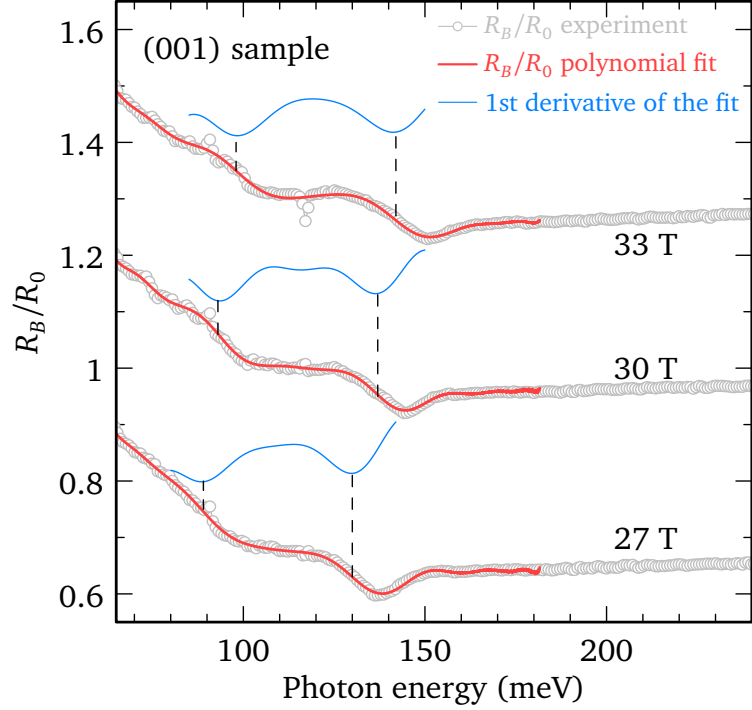


Fig. S7. Relative magneto-reflectivity spectra of the (001)-oriented sample taken at $B = 27, 30$ and 33 T (gray circles), fitted using a high-order polynomial function (red curves). The points of inflections, associated with the position of two CR modes, are taken as minima in the first derivative of the polynomial fit (blue curves).

Even though these additional data and the detailed analysis provide us with compelling evidence for the existence of the satellite lines, we remain conservative in our conclusions and denote their existence in our manuscript as *likely* but still not fully confirmed. Their existence merely gives a supporting argument in the interpretation of our data. The main conclusions are drawn based on the analysis of the clearly resolved main CR modes.

MAGNETO-TRANSPORT CHARACTERIZATION OF THE STUDIED SAMPLES

Cd_3As_2 samples studied in our (magneto-)optical experiments were also characterized using the low-field magneto-transport technique. The electrical contacts were deposited using silver paste, which allowed us to probe the longitudinal magneto-resistance $R_{xx}(B)$ in a four-contact configuration. Further quantities, such as resistivity or carrier mobility, could not be deduced with a sufficient precision due to fairly irregular shape of samples, showing only one well-defined facet explored in our reflectivity study. The magnetic field was always applied perpendicular to the optical facets.

A summary of results from the (001)-oriented sample is presented in Figs. S8a-c. In line with previous experiments performed on samples from the same source [14], the longitudinal magneto-resistance R_{xx} increases almost linearly with B in the range of applied magnetic fields. Shubnikov-de Haas oscillations emerge in the background-removed data $\Delta R_{xx}(B)$ at $B \approx 2$ T (inset of Fig. S8a). They imply a single dominant oscillation frequency, $B_f \approx 37$ T, obtained when a fast Fourier transformation is applied to $\Delta R_{xx}(1/B)$, see Fig. S8b.

The deduced frequency $B_f \approx 37$ T perfectly matches our expectations based on the analysis of the optical data. The Fermi surface cross section of an ideal conical band $A = \pi E_F^2 / (v^2 \hbar^2)$ yields the oscillation frequency $B_f = \hbar A / (2\pi e) = E_F^2 / (2e\hbar v^2)$. Taking the Fermi energy estimated for the (001)-oriented sample from the onset of interband absorption, $E_F^{001} \approx 200$ meV, and the band velocity, $v = 0.93 \times 10^6$ m/s, deduced from our CR modes, we obtain $B_f \approx 35$ T.

The damping of the quantum oscillations with temperature (the inset of Fig. S8a), which was analyzed using the standard Lifshitz-Kosevich formalism, brings another consistency check of our interpretation. A closer look at the damping of the amplitude at $B = 6.6$ T (Fig. S8c) implies the effective mass at the Fermi level of $m_{001} = 0.036m_0$.

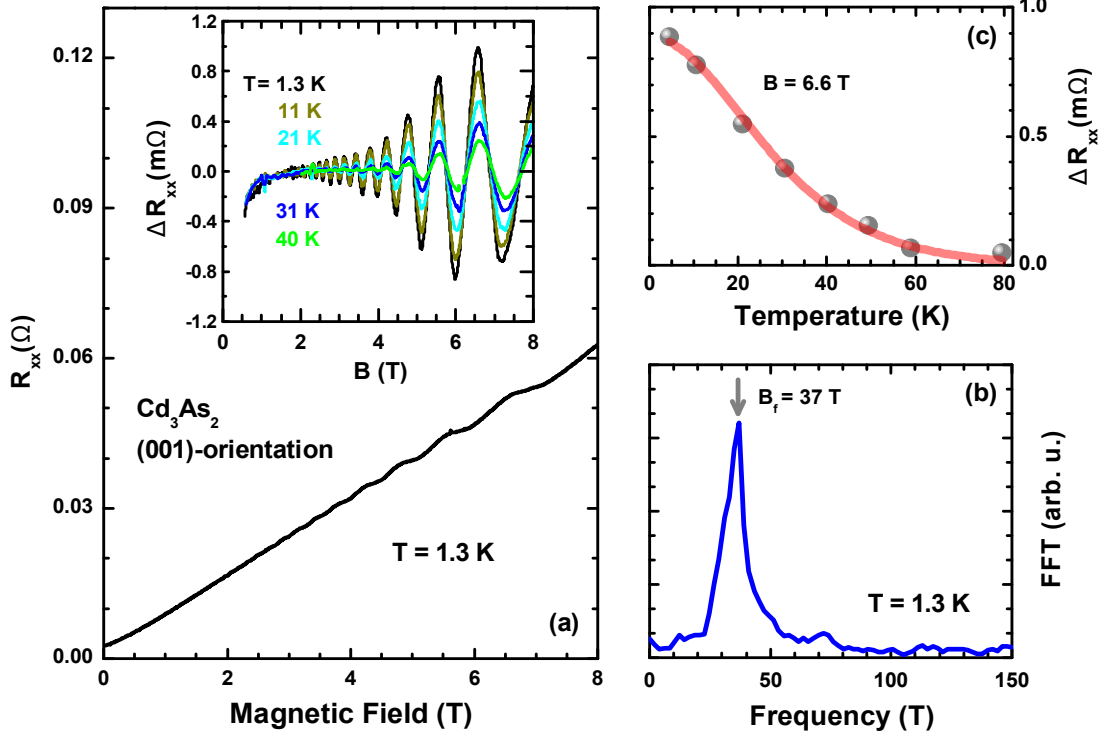


Fig. S8. The results of magneto-transport experiments performed on (001)-oriented sample. (a) Longitudinal magneto-resistivity $R_{xx}(B)$ measured at $T = 1.3$ K with quantum oscillations superimposed on nearly linear in B background. The background-removed longitudinal resistivity traces $\Delta R_{xx}(B)$ measured at $T = 1.3, 11, 21, 31$ and 40 K are plotted in the inset. (b) a fast Fourier-transform of $\Delta R_{xx}(1/B)$ showing a clear periodicity of the observed oscillations in $1/B$ with a dominant frequency of $B_f = 37$ T. (c) Temperature dependence of the ΔR_{xx} amplitude at $B = 6.6$ T, implying the effective mass $m \approx 0.036m_0$ at the Fermi level.

This agrees well with the effective mass expected theoretically, $m = E_F/v^2 = 0.041m_0$, as well as that estimated from the plasma edge splitting at low magnetic fields, $m_{001} = 0.04m_0$ (Fig. S4a).

In contrast to the (001)-oriented sample, the magneto-transport experiments carried out on the (112)-oriented sample did not bring any conclusive results. The main obstacle was preparing reliable ohmic electrical contacts for this low doped sample, where the carrier density estimated from the optical conductivity is as low as $n \sim 10^{17} \text{ cm}^{-3}$.

INFLUENCE OF THE SPIN-ORBIT COUPLING STRENGTH

In the main part of the manuscript, the strength of the spin-orbit coupling in Cd_3As_2 was fixed at the value known for another arsenic-based semiconductor InAs , $\Delta = 400$ meV. Due to the limited space, we did not discuss in detail its influence on the presented modeling. Here we show that a reasonable variation of Δ does not imply any dramatic changes in the theoretically calculated positions of CR modes. We illustrate this in Fig. S9, where the experimentally deduced CR energies are plotted against their theoretically expected positions for particularly weak and strong values of Δ . The velocity parameter was kept constant at $v = 0.93 \times 10^6$ m/s in these calculations. We may also note that the zero-field response of Cd_3As_2 is consistent with the spin-orbit coupling close to 400 meV or lower. Higher values would, according to the formula (S24), suppress the theoretically expected strength of the interband absorption in the middle infrared range and worsen agreement with our experimental data (in Fig. 1b in the main text).

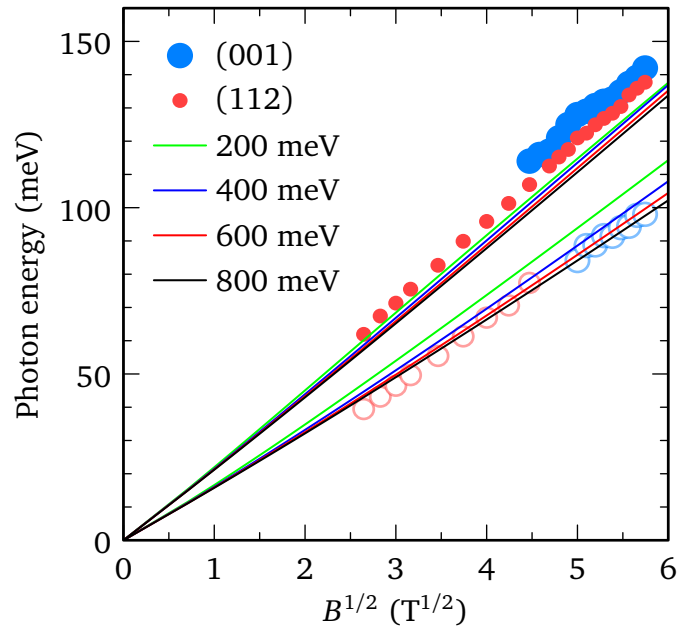


Fig. S9. The fan chart of observed CR modes in the (001)- and (112)-oriented sample compared to theoretically expected positions calculated within the gapless Kane model for various strength of the spin-orbit coupling $\Delta = 200, 400, 600$ and 800 meV while keeping the velocity parameter $v = 0.93 \times 10^6$ m/s constant.

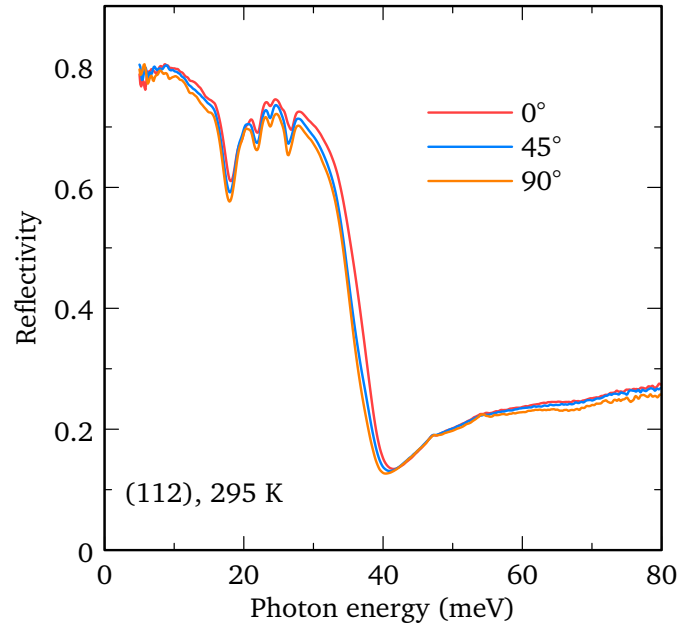


Fig. S10. Room-temperature reflectivity spectra of the (112)-oriented sample measured with linearly polarized radiation. Nearly identical response for three different orientations of the light polarization plane, encompassing two principal axes separated by 90° , implies very high isotropy of the optical response of Cd_3As_2 . A gold mirror (not in-situ overcoating technique) was used as a reference for reflectivity measurements presented in this figure.

REFLECTIVITY OF THE (112)-ORIENTED SAMPLE – ANISOTROPY OF THE OPTICAL RESPONSE

To estimate the degree of anisotropy in Cd_3As_2 , we have performed a polarization-dependent measurement of the reflectivity for the (112)-oriented sample. In principle, the (112) facet may be optically anisotropic. The polarization

plane was rotated with respect to an arbitrarily chosen axis on the sample surface. Fig. S10 shows the spectra obtained for two principal optical axes, separated by 90° , and an angle in between. The shift in the plasma edge is close to 1 meV. This experiment provides us with another piece of evidence for high isotropy of the electronic bands in Cd_3As_2 .

* milan.orlita@lncmi.cnrs.fr

- [1] J. Bodnar, in *Proc. III Conf. Narrow-Gap Semiconductors, Warsaw*, edited by J. Rauluszkiewicz, M. Górska, and E. Kaczmarek (Elsevier, 1977) p. 311.
- [2] H. Kildal, *Phys. Rev. B* **10**, 5082 (1974).
- [3] E. O. Kane, *J. Phys. Chem. Solids* **1**, 249 (1957).
- [4] M. Orlita, D. M. Basko, M. S. Zholudev, F. Teppe, W. Knap, *et al.*, *Nature Phys.* **10**, 233 (2014).
- [5] P. R. Wallace, *phys. stat. sol. (b)* **92**, 49 (1979).
- [6] M. König, S. Wiedmann, C. Brüne, A. Roth, H. Buhmann, L. W. Molenkamp, X.-L. Qi, and S.-C. Zhang, *Science* **318**, 766 (2007).
- [7] P. E. C. Ashby and J. P. Carbotte, *Phys. Rev. B* **87**, 245131 (2013).
- [8] A. R. Wright and R. H. McKenzie, *Phys. Rev. B* **87**, 085411 (2013).
- [9] A. Raoux, M. Morigi, J.-N. Fuchs, F. Piéchon, and G. Montambaux, *Phys. Rev. Lett.* **112**, 026402 (2014).
- [10] M. O. Goerbig, G. Montambaux, and F. Piéchon, *EPL (Europhysics Letters)* **105**, 57005 (2014).
- [11] M. N. Ali, Q. Gibson, S. Jeon, B. B. Zhou, A. Yazdani, and R. J. Cava, *Inorganic Chemistry* **53**, 4062 (2014).
- [12] H. Schleijsen, M. von Ortenberg, M. Gelten, and F. Blom, *Int. J. Infrared Milli.* **5**, 171 (1984).
- [13] E. D. Palik and J. Furdyna, *Rep. Prog. Phys.* **33**, 1193 (1970).
- [14] T. Liang, Q. Gibson, M. N. Ali, M. Liu, R. J. Cava, and N. P. Ong, *Nature Mater.* **14**, 280 (2015).